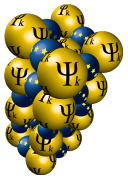

Ψ_k **Scientific Highlight Of The Month**

No. 143 **November 2018**

Electronic correlations in iron under extreme conditions

Leonid V. Pourovskii[1]

CPHT, Ecole Polytechnique, CNRS, Université Paris-Saclay, Route de Saclay, 91128 Palaiseau, France

Collège de France, 11 place Marcelin Berthelot, 75005 Paris, France

Abstract

We discuss the role of dynamical many-electron effects in the physics of iron and iron-rich alloys at high-pressure/high-temperature conditions on the basis of recent *ab initio* studies employing the dynamical mean-field theory. After reviewing previous applications of this theory to iron at the ambient pressure, we first focus on the moderate-pressure range up to 60 GPa and low temperatures. The electronic mass enhancement and scattering rate are found to be significantly enhanced at the pressure-induced transition between ground-state ferromagnetic body-centered-cubic α-Fe and hexagonal close-packed paramagnetic ϵ-Fe resulting in a step-wise increase of the electrical resistivity and a significant correction to the ϵ-Fe equation of state. The disappearance of magnetic order at the α-ϵ transition is the cause of this enhancement with dynamical correlations suppressed by a large spin polarization in the α-phase. An electronic topological transition is predicted to be induced in ϵ-Fe by many-electron effects; its signatures are experimentally observed in this phase at the pressure of about 40 GPa. Next section focuses on the geophysically relevant pressure-temperature regime of the Earth's inner core (EIC). The three iron allotropes (α, ϵ and face-centered-cubic γ) considered as possible stable phases at such conditions feature qualitatively different many-electron effects as evidenced, e. g., by a strongly non-Fermi-liquid metallic state of α-Fe and an almost perfect Fermi liquid in the case of ϵ-Fe. A recent active discussion on the electronic state and transport properties of ϵ-Fe at the EIC conditions is reviewed in details. We also discuss the impact of a Ni admixture, which is expected to be present in the core matter. We conclude by outlining some limitation of the present DMFT-based framework relevant for studies of iron-base systems as well as perspective directions for further development. Key features of this theoretical framework are reviewed in some details in the Appendix.

[1]leonid@cpht.polytechnique.fr

Contents

1 Introduction **2**

2 ϵ-Fe under moderate pressure: equation of state, resistivity and electronic topological transitions **5**

3 Many-electron effects in iron and iron-nickel alloy at the Earth's inner core conditions **10**

3.1 Electronic structure and magnetic susceptibility of iron and iron-nickel alloys . . 12

3.2 Electron-electron scattering and transport in ϵ-Fe 18

3.3 Many-electron effects and structural stability 21

4 Conclusions and perspectives **22**

A *Ab initio* dynamical mean-field theory approach: an overview **25**

A.1 Dynamical mean-field theory 28

A.2 The quantum impurity problem 30

A.3 Charge density and total energy 32

B The impact of density-density approximation: a benchmark **34**

1 Introduction

Iron is a key material for our civilization since the advent of "Iron Age" at about 1000 BC. The technological utility of iron originates in a vast phase space provided by iron-based alloys, allowing for divers microstructures to be produced with small variations in the composition and an appropriate thermal treatment. In particular, the rich zoo of steels is composed by three stable phases - the ferrite (body-centered cubic, bcc, α) austenite (face-centered cubic, fcc, γ) and cementite (orthorhombic carbide Fe_3C) - in addition to various metastable phases, for example, the body-centered tetragonal martensite α' (see, e.g., [1]). This multitude of phases observed in iron-based alloys and compounds stems from the complex physics of pure iron, which features three distinct allotropes at the ambient pressure: ground-states bcc α-Fe transforms into fcc γ-Fe at 1185 K; the fcc phase subsequently transforms to yet another bcc phase, δ-Fe, at 1667 K. Though α and δ-Fe have the same bcc crystal structure, their physics is quite different, with the vibrational entropy believed to be playing the key role in stabilization of the later [2]. Iron is a classic itinerant ferromagnet, and the ferromagnetic order is well recognized to be crucial in stabilizing α-Fe [3]. However, as noted above, the α phase still exists above the Curie temperature of 1044 K. The fcc γ phase is paramagnetic in its bulk form stable only at high-temperatures. However, γ-Fe can be stabilized in small precipitates in an fcc matrix, e.g., in Cu, down to zero temperature, and at low temperatures it exhibits a complex non-commensurate

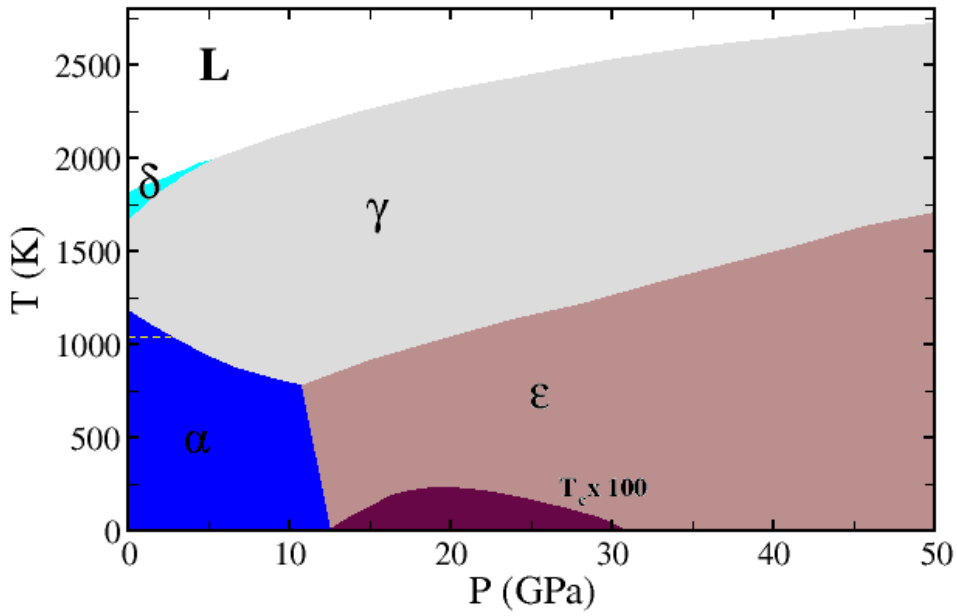

Figure 1: The pressure-temperature phase diagram of iron in the moderate pressure range up to 50 GPa. The superconducting transition temperature for ϵ-Fe is multiplied by 100. The yellow horizontal dashed line in the α-Fe region indicates its ferromagnetic T_c.

antiferromagnetic order [4].

Under applied pressure above 10 GPa α-Fe transforms into another allotrope, hexagonal close-packed (hcp) ϵ-Fe [5, 6]. This phase is found to be stable at room temperature up to the highest pressure reached to date [7]; *ab initio* density-functional-theory (DFT) calculations predict iron to remain in the ϵ phase up to a pressure of the order of 10 TPa [8]. Experimental studies of ϵ-Fe under moderate pressures reveal a superconducting dome in the range of pressure from 10 to 30 GPa with the maximum value of superconducting T_c of about 2 K [9]; this superconductivity is likely of non-conventional nature and mediated by spin-fluctuations [10]. No magnetic order has been detected in ϵ-Fe down to temperatures as low as 8 K [11, 12]. A puzzling non-Fermi-liquid (nFL) temperature scaling $\propto T^{5/3}$ of the low-temperature resistivity of ϵ-Fe was also reported [13, 14].

This rich phase diagram (Fig. 1) with several allotropes exhibiting various magnetic orders, a non-conventional superconductivity as well as instances of a nFL behavior in the ϵ-phase hint at a complex many-electron physics of iron metal. Many-electron effects in iron are expected to arise due to the on-site Coulomb repulsion between rather localized $3d$ states hybridized with itinerant $4s$ bands. The typical width W of the iron $3d$ band is in the range of 5 to 6 eV for the ambient-moderate pressure range; the estimated value of the local Coulomb interaction parameter U (Slater F^0) is in the range from 2.3 to 6 eV, in accordance with constrained local-density approximation [15, 16, 17] and constrained random-phase approximation [18, 19] calculations (see Appendix A for a short overview of these methods). In spite of a large spread in the theoretical estimates of U, one may conclude that the ratio U/W in Fe is less than or equal to 1. Taking into account only the effect of $U \leq W$ one would expect rather weak electronic correlation effects in a multiband system away from half-filling [20]. Indeed, the strength of

electronic correlations in iron is found to be much more sensitive to Hund's coupling J_H, which value is in the range of 0.85 to 1 eV. In this respect the physics of iron is close to that of "Hund's metals" [21, 22, 23], in which the strength of correlations away from half-filling is determined mainly by J_H. In particular, model studies point out to a key role of J_H in stabilizing the ferromagnetic phase in multiband systems away from half-filling [24]. Another important aspect is the interplay between the local Coulomb interaction, characterized by large J_H, and crystal-field splitting of Fe $3d$ states. This interplay is particularly striking in the bcc α phase, where the partial e_g density-of-states (DOS) features a large peak pinned at the Fermi level due to a van Hove singularity [25, 26]. Correspondingly, this high DOS at the Fermi level in nonmagnetic α-Fe explains its tendency towards the ferromagnetism in accordance with the Stoner criterion.

The Stoner ferromagnetism of α-Fe is well captured by density functional theory (DFT) calculations in conjunction with the local spin-density approximation (LSDA) exchange-correlation functional predicting the theoretical ordered moment of 2.2 μ_B that agrees well with experiment. Though DFT-LSDA incorrectly predicts γ-Fe to be the ground states [27], this error is corrected by semi-local exchange-correlation potentials like generalized gradient approximation (GGA) [28, 29]. However, the existence of paramagnetic bcc phase is a significant challenge for density functional theory. Direct DFT calculations predict too small volume and too high bulk modulus for non-magnetic α-Fe; moreover, this non-magnetic phase is mechanically and dynamically unstable within DFT [30, 31], in clear disagreement with experiment. DFT calculations predict paramagnetic γ-phase to be dynamically unstable as well [31]. A number of methods has been developed in the DFT framework to remedy its deficiency in describing paramagnetic phases. Several such techniques were subsequently applied to iron, like the disordered local moments (DLM) method [32, 33, 34], the spin-statistical-averaging method of Körmann *et al.* [35], or the spin-wave approach of [36], for a recent review of those techniques see, e.g., [37]. The spin-disorder contribution to the resistivity of iron at ambient and extreme conditions has been also evaluated using such DFT-based methods [38, 39]. However, these techniques represent the paramagnetic state by a certain combination of systems with static local moments; their applicability to the cases like ϵ-Fe, where no static magnetic order or local-moment behavior is observed at any T, is not obvious. Moreover, such approaches are typically useful to describe the thermodynamics of local-moment paramagnets, but they are not designed to capture their spectral properties. And even for ferromagnetic α-Fe the DFT electronic structure is only in a rough qualitative agreement with experimental photoemission spectra, missing, in particular, the observed quasiparticle renormalization of the $3d$ bands by 40-50% and a lifetime damping of quasiparticle states [40] .

This inability of pure DFT to fully capture the physics of iron at ambient condition, in particular, of high-temperature paramagnetic α-Fe as well as the γ and δ phases has prompted a number of theoretical studies of this system employing a combination of DFT with a dynamical mean-field theory (DMFT) treatment of the narrow $3d$ iron band.

In particular, Leonov and coworkers applied this DFT+DMFT approach in conjunction with a quantum Monte Carlo impurity solver to obtain total energies and phonon dispersions in paramagnetic α and γ phases [41, 31]. Their calculations predicting dynamically and thermodynamically stable paramagnetic α-Fe in the range of temperatures from T_c to $1.3T_c$, in qualitative agreement with experimental phase diagram. Leonov *et al.* have subsequently extended their

phonon-dispersion calculations of the bcc phase to the temperature range of existence of δ-Fe [42] finding it dynamically unstable in the harmonic approximation, this result was very recently challenged by another DFT+DMFT study [43]. Theoretical DFT+DMFT calculations of the one-electron spectra of iron [44, 45, 46, 47, 48, 49, 43] have been mostly confined to the ferromagnetic α phase, for which experimental angular-resolved photoemission (ARPES) spectra are available [40, 48]. Refs. [50] and [51] also studied the one-electron spectral function and magnetic susceptibilities of the paramagnetic α and γ phases. Sánchez-Barriga *et al.* [48] concluded that a purely-local single-site DMFT self-energy is not sufficient to obtain a quantitative agreement between the theoretical **k**-resolved spectral function and experimental ARPES spectra, though they employed an approximate treatment of the DMFT quantum impurity problem. The most recent DFT+DMFT studies [49, 43] employing a numerically-exact quantum Monte Carlo approach [52] obtain a reasonable quantitative agreement with ARPES, though discrepancies for some high-symmetry directions are still present. The same level of agreement was obtained by including both local non-local many-electron effects within a weak-coupling quasiparticle GW approach [53]. Hence, a combination of non-perturbative treatment of the on-site correlations with a weak-coupling approach to non-local ones (see, e.g., Refs. [54, 55]) is probably necessary to fully account for one-electron spectra of ferromagnetic α-Fe.

Correlation effects in iron under moderate and high pressure have been comparatively less studied with DFT+DMFT until recently. The present highlight focuses on this topic, reviewing, in particular, new theoretical results obtained during the last 5 years. First, we consider the hcp ϵ phase, which puzzling ground-state and transport properties in the moderate pressure range of 10 to 60 GPa were shortly described above. The subsequent section deals with properties of the α, γ and ϵ iron and iron-nickel alloy at the volume of 7.05 Å/atom and at temperatures up to 6000 K. These density and temperature are expected for the inner core of Earth, hence, the phase stability and transport properties of iron at such conditions are of a particular relevance to the geophysics. Though high density is expected to diminish the relative importance of potential energy, we still find a rather significant impact of the local interaction between $3d$ electrons on the electronic structure, phase stability as well as on magnetic and transport properties. In order to make this highlight self-contained we also succinctly review the DFT+DMFT framework in Appendix A.

2 ϵ-Fe under moderate pressure: equation of state, resistivity and electronic topological transitions

As noted above, DFT successfully captures the magnetic state α-Fe; DFT calculations also predict the ground-state properties of this phase in good agreement with experiment. In contrast, the same theory fails to account even for basic ground-state properties of ϵ-Fe. Within the local spin-density and generalized gradient approximations for the exchange-correlation potential it predicts a rather strong antiferromagnetism, with the iron moment of about 1.5 μ_B at the volume of 73 $(\text{a.u.})^3$/atom, corresponding to that of the ϵ-phase at the $\alpha \rightarrow \epsilon$ transition point [56]. No antiferromagnetic phase has been observed experimentally in ϵ-Fe down to 8 K [11, 12] (though [57] observed a magnetic signal in X-ray emission spectroscopy, which they ascribed to

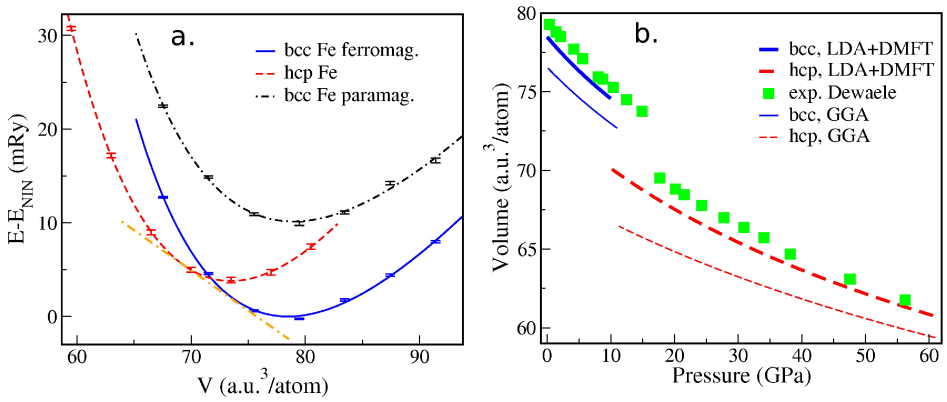

Figure 2: a). DFT+DMFT total energy vs. volume per atom for α (ferromagnetic, solid blue line, and paramagnetic, dot-dashed black line) and ϵ (dashed red line) Fe. The error bars are the CT-QMC method stochastic error. The orange long dash-dotted straight line indicates the common tangent construction for the $\alpha - \epsilon$ transition. b). Equations of states (EOS) for ferromagnetic α (low pressure) and paramagnetic ϵ (high pressure) Fe. Theoretical results are obtained by fitting the DFT+DMFT (thick line) and GGA (thin line) total energies, respectively, using the Birch-Murnaghan EOS. The experimental EOS of iron shown by green filled squares is from [60]. Adapted from Ref. [61].

anitferromagnetic fluctuations). If the nonmagnetic ground state is imposed, DFT total energy calculations predict an equation of state that drastically disagrees with experiment. The bulk modulus is overestimated by more than 50%, and the equilibrium volume is underestimated by 10% compared to the experimental values [58]. Another puzzling experimental observation is a large enhancement in the resistivity across the α-ϵ transition. The room temperature total resistivity of ϵ-Fe is twice as large as that of the α phase [13]. The electron-phonon-scattering contribution to resistivity calculated within GGA is in excellent agreement with the experimental total resistivity for the α phase [59], however, these calculations predict virtually no change in the resistivity across the transition to antiferromagnetic hcp-Fe. All these discrepancies between DFT calculations and experiment point out to a possible important role of dynamic correlations in ϵ-Fe.

The evolution of electronic correlations across the $\alpha \rightarrow \epsilon$ transition as well as its impact on the equation of state and electrical resistivity were studied by Pourovskii *et al.* [61] using a self-consistent DFT+DMFT approach; the quantum impurity problem was solved using the hybridization-expansion CT-QMC method briefly introduced in Appendix Sec. A.2. In order to achieve the necessary accuracy with a manageable computational cost the non-density-density terms in the Coulomb vertex were neglected, see Appendix B. This local Coulomb interaction vertex between Fe $3d$ states was parametrized by $U = F^0$ =4.3 eV and J_H=1 eV. These values of the interaction parameters were chosen on the basis of the previous cRPA calculations for iron by [19]; their value of U =3.4 eV for α-Fe was increased by about 25% to effectively account for the high-frequency tails of the Coulomb vertex [62]. The value of J_H was fixed at the top of the accepted range of 0.85 to 1.0 eV to reproduce the value of magnetic moment in α-Fe at the ambient conditions.

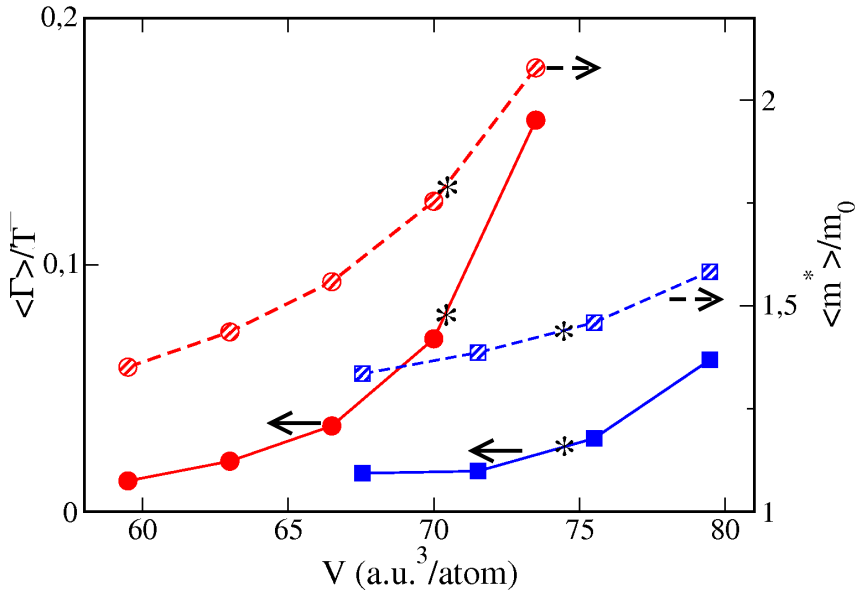

Figure 3: The ratio of averaged over orbitals inverse quasiparticle lifetime $\langle\Gamma\rangle$ to temperature (the left axis) and the analogously averaged mass enhancement $\langle m^*\rangle/m_0$ (the right axis) vs. volume per atom. The solid lines (filled symbols) and dashed lines (hatched symbols) are $\langle\Gamma\rangle/T$ and $\langle m^*\rangle/m_0$, respectively. The values for α and ϵ phases are shown by blue squares and red circles, respectively. The black stars indicated their corresponding atomic volumes at the transition point. Adapted from Ref. [61].

Overall, DFT+DMFT total energy calculations of Ref. [61] provide a comprehensive and quantitatively correct picture for the ground-state properties of both phases including their ground-state volumes, bulk moduli as well as the pressure dependence of the c/a ratio in ϵ-Fe. In particular, they predict a ferromagnetic α-Fe ground state and a transition $\alpha \rightarrow \epsilon$ phase at 10 GPa, in agreement with experiment (Fig. 2a). The calculated difference in total energy between the ferromagnetic and paramagnetic states of α-Fe is of about 10 mRy (1500 K), in a good correspondence to its experimental Curie temperature of 1043 K. The Birch-Murnaghan equations of states (EOS) fitted to DFT+DMFT total energies of α and ϵ-Fe agree well with the corresponding experimental EOS (Fig. 2b). One observes a particularly significant improvement for the case of ϵ-Fe, for which the DFT-GGA framework performs quite poorly. In contrast, the DFT+DMFT corrections to EOS of ferromagnetic α-Fe are rather small; as noted in Sec. 1, the DFT in conjunction with GGA already describes the ground-state properties of this phase quite well.

The fact that many-body corrections to the ground-state properties are much more significant in the case of ϵ-Fe as compared to α-Fe hints at stronger dynamic electronic correlations in the former. Indeed, the mass enhancement $m^*_a/m_0 = Z_a^{-1}$ and the inverse quasiparticle lifetime

$$\Gamma_a = -Z_a \Im\Sigma_a(\omega = 0), \tag{1}$$

where a is the m and spin quantum numbers labeling Fe $3d$ orbitals, $Z_a = [1 - d\Im\Sigma_a(i\omega)/d\omega|_{\omega\rightarrow 0}]$ is the quasiparticle residue extracted from the zero-frequency value of the DMFT self-energy

Σ_a (see Appendix Sec. A.1) for the orbital a, exhibit a large increase at the $\alpha \rightarrow \epsilon$ transition (Fig. 3). This enhancement of dynamic correlations is due to the suppression of the static magnetic order at this transition. In fact, paramagnetic α-Fe is a strongly-correlated nFL system, with a particularly large value of Γ for localized e_g states [50, 63]. In contrast, only a modest Fermi-liquid renormalization of Fe $3d$ DFT band structure is detected by ARPES for the ferromagnetic phase [40]; their value for the mass enhancement of about 40-50% agrees reasonably with the DFT+DMFT prediction of 1.6 for $\langle m^* \rangle$ for the ambient conditions (Fig. 3).

A step-wise increase of the inverse quasiparticle lifetime Γ at the $\alpha \rightarrow \epsilon$ transition point should result in a corresponding step-wise increase of the electron-electron-scattering contribution to the electrical resistivity. Indeed, DFT+DMFT calculations for the transport presented in the same paper [1] predict such a jump with the electron-electron contribution enhanced by a factor of 3, from 0.5 $\mu\Omega$·cm in α-Fe to 1.5 $\mu\Omega$·cm in the ϵ phase. The jump in total resistivity ρ at the transition observed experimentally [13, 14] features an overall qualitative shape of the resistivity vs. pressure in iron strongly resembling the DFT+DMFT one. However, the experimental jump in ρ at the $\alpha \rightarrow \epsilon$ transition for the room temperature is an order of magnitude larger than 1 $\mu\Omega$·cm predicted by our calculations. The present approach, apparently, misses the main source of this resistivity enhancement. The fact that the resistivity jump is still well resolved at T =4 K lends a strong support to its electron-electron-scattering origin. A strongly nFL behavior of ϵ-Fe in the temperature range from 2 to (at least) 30 K, in conjunction with a non-conventional superconducting state at lower T points out at important intersite correlations, e.g. spin fluctuations, which are neglected by the single-site DFT+DMFT framework. Alternatively, one may suggest that local non-density-density interaction terms (see Appendix A.2 and B) neglected in Ref. [61] have a crucial impact on the low-energy behavior of the self-energy $\Sigma(\omega)$ and, hence, at the transport. This problem is an interesting subject for future works.

No experimental ARPES of ϵ-Fe has been reported to date due to the obvious difficulty of performing such measurements at a high pressure of tens GPa. Glazyrin *et al.* [64] studied the impact of pressure on the electronic structure of the ϵ phase by measuring a set of quantities readily accessible at high pressure conditions, namely, the Debye sound velocity, Mössbauer central shift and hexagonal cell c/a ratio, in pure Fe and in $Fe_{0.9}Ni_{0.1}$. All three quantities are found to exhibit a distinct peculiarity at about 40 GPa. One sees, for example, a clear change of slope in the evolution of c/a vs. P as well as a peculiarity in the Mössbauer central shift at this pressure, which is especially pronounced in the case of $Fe_{0.9}Ni_{0.1}$ (Fig. 4). As discussed by [64] peculiarities simultaneously appearing in all three quantities can be qualitatively explained by an electronic topological transition (ETT) due to the appearance of new Fermi-surface hole pockets at a given pressure [65, 66, 67]. The resulting peculiarities in these quantities are proportional to the change of DOS at the Fermi level, $\delta N(E_F)$, due to the ETT.

In order to precisely identify the ETT at the origin of observed peculiarities Ref. [64] calculated the DFT+DMFT $\mathbf{k}$-resolved spectral function $A(\mathbf{k}, \omega) = -\frac{1}{\pi}\Im G(\mathbf{k}, \omega + i\delta))$ from the analytically-continued lattice Green's function (GF), eq. 9 in Appendix A.1, as a function of volume. $A(\mathbf{k}, \omega)$ obtained by DFT+DMFT clearly features the emergence of new hole pockets at the Γ and L high symmetry point (Fig. 5a and 5b). The corresponding critical pressure for the ETT is found

[1] See Sec. 3.2 for a brief summary of the formalism for transport calculations

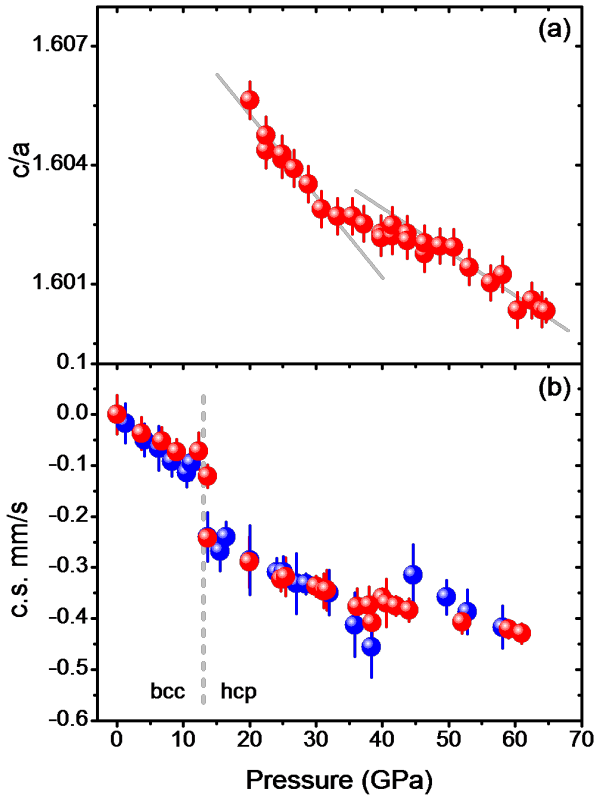

Figure 4: Experimental pressure dependence of (a) hcp phase c/a ratio and (b) the Mössbauer centre shift based on several experimental datasets for pure iron (red circles) and for $Fe_{0.9}Ni_{0.1}$ alloy (blue circles). The centre shift values are given relative to pure α iron. Straight grey lines in (a) are guides for the eye. Adapted from Ref. [64].

to be in the range of 40-80 GPa, depending on the chosen value of U. In contrast, the DFT band structure features those hole pockets (Fig. 5d) already at 10.4 Å^3/at, which is the atomic volume of ϵ-Fe at the $\alpha \rightarrow \epsilon$ transition. Hence, DFT does not predict any ETT to occur in the ϵ phase in its experimental range of existence.

This significant shift of ETT to lower volumes/higher pressures in DFT+DMFT compared to pure DFT are mainly due to many-electron corrections to the overall position of the valence d bands with respect to the s ones, leading to a relative shift of states with a significant s contribution with respect to the rest. A similar significant impact of many-body corrections was recently predicted even for such weakly correlated system as the osmium metal by Feng *et al.* [68]. They found the transition pressures for a series of ETTs to be in a better agreement with experiment when DMFT corrections were included. One may notice, however, that the relative shift of "correlated" d vs. "uncorrelated" s states is sensitive to the choice of the double-counting (DC)correction (see Appendix A). Both Refs. [61] and [68] employ the "around mean-field" form of DC, which is believed to be appropriate for such relatively itinerant systems.

On the experimental side, Dewaele and Garbarino [69] have very recently reported new measurements of the equation of state and c/a ratio of ϵ-Fe. The experimental equation of state

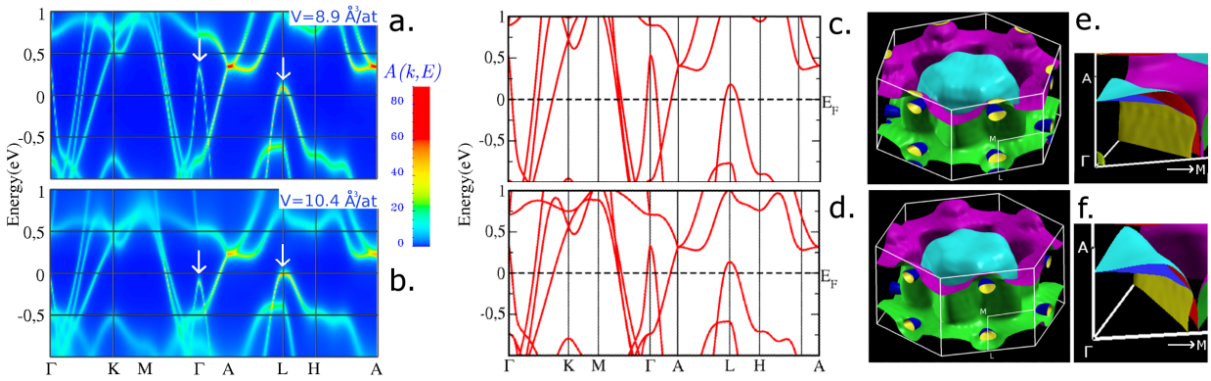

Figure 5: The DFT+DMFT **k**-resolved spectral function $A(\mathbf{k},\omega)$ (in units of V_{at}/eV, where V_{at} is the volume per atom) of ϵ-Fe at volumes V_{at} of 8.9 Å^3/atom (a) and 10.4 Å^3/atom (b) corresponding to pressures of 69 and 15.4 GPa, respectively. The energy zero is taken at the Fermi level. The hole-like bands at the Γ and L points at volume 8.9 Å^3/atom (indicated by the white arrows) are below E_F at V=10.4 Å^3/atom. The corresponding DFT band structures are shown in c and d, respectively. The corresponding DFT+DMFT Fermi surfaces for two volumes are shown in e and f, respectively. Adapted from Ref. [64].

is found to be in good agreement with calculations of Ref. [61]. Though no sign of peculiarity was observed in the c/a ratio by Ref. [69], one may notice that the scatter of their points is significantly larger than that of Glazyrin *et al.* [64].

3 Many-electron effects in iron and iron-nickel alloy at the Earth's inner core conditions

The wealth of available data on seismic wave propagation, planetary density and gravitational field, abundance of elements in the Solar system lends strong support to the hypothesis of iron being one of principal component of Earth and Earth-like planets [70, 71, 72]. In particular, the solid inner and liquid outer cores of Earth are believed to consist mainly of iron. The measured Earth interior density profile as well as data on the meteorite composition favor a picture of a solid Earth's inner core (EIC) composed of iron alloyed with about 10% of nickel and non-negligible quantities of light elements like Si, S, or O. Inside the EIC the matter is subjected to pressure P in the range of 330 to 360 GPa at temperature T of about 6000 K, though the relevant range of T for the inner core is still actively debated [73, 74, 75]. The temperature of solid phase inside EIC is close to its melting point. The phase stability and properties of solid iron and iron-rich alloys at such extreme conditions are of high importance for the geophysics as they represent a key input to geophysical models of Earth's core dynamics and its evolution. In particular, the interpretation of seismic data is largely based on the assumed phase diagram for relevant iron-rich alloys at the core's conditions [76]. The models of core evolution in time are constrained by the accepted range of values for the thermal and electrical conductivities [77, 78]. Therefore, significant research efforts, both experimental and theoretical, are focused on reliably determining the nature of Fe phases stable in the relevant (P,T) range

and their physical properties.

Iron and its alloys at extreme conditions have been studied experimentally using the dynamical shock-wave compression and, more recently, with the static heated diamond anvil cell method. As noted in the previous section, these studies have established the stability of ϵ-Fe up to the pressure range of EIC at the room temperature [7]. The situation is less clear for the high-T region, where some recent experiment [79, 80, 81] found the ϵ-phase to remain stable in the relevant pressure range up to the EIC temperatures, while other studies [82, 83] observed bcc α-Fe to emerge at high temperatures approaching the melting point. Tateno *et al.* [79] claimed to reach the EIC conditions and observed only the ϵ phase in the studied range of P from 100 GPa to the highest pressure of 377 GPa and T from 2000 to 5700 K. However, their interpretation of the data was subsequently disputed by Dubrovinsky *et al.* [84], who suggested that the EIC temperature was not in fact reached by Ref. [79]. Overall, currently there is no experimental consensus regarding the stable phase of Fe at EIC conditions.

The theory input is particularly valuable in such situation, hence, a number of DFT based simulations of Fe and its alloy has been published in the last two decades. These studies treated lattice vibrations in the quasi-harmonic approximation [85, 8] or with the full *ab initio* molecular dynamics approach [86, 87, 88]. The results of these calculations are also inconclusive, with all three known phase of iron predicted to be stable at EIC conditions by different authors. The difference in DFT free energy between those phases is found to be decreasing with increasing temperature and pressure. Thus the relative stability becomes sensitive to small differences in the calculational setup like the size of simulation supercell or the density of **k**-mesh employed in the Brillouin zone integration [87, 88]. In particular, the non-magnetic α phase dynamically unstable at low temperature is claimed by Belonoshko *et al.* [88] to be stabilized by an unconventional high-T diffusion mechanism; in contrast, Godwal *et al.* [87] found α-Fe to be dynamically unstable at the EIC conditions. The free-energy difference between γ and ϵ-Fe becomes extremely small close to the melting temperature in accordance with Ref. [85], who predicted γ-Fe to be stable at the EIC conditions, while Stixrude [8] found the ϵ-phase to be more stable. In all these *ab initio* simulations the standard DFT framework in the conjunction with LDA or GGA exchange-correlation potential was employed thus neglecting dynamical correlation effects. This approximation is usually justified (see, e. g., Ref. [8]) by the fact that the local Coulomb repulsion U between iron $3d$ states is smaller than the effective $3d$ bandwidth, especially at high pressure. Though this statement is correct even at the ambient pressure, this does not mean that correlation effects in iron are negligible. As noted in the previous section, the strength of local many-electron effects in iron is much more sensitive to the Hund's rule coupling J_H, which is expected to be quite insensitive to pressure. High temperature stabilizing high-entropy states may strengthen the tendency towards a nFL behavior or the formation of local magneitc moments. Hence, the role of many-electron effects needs to be evaluated with explicit calculations.

This problem was addressed in Ref. [63] by DFT+DMFT calculations for the all three phases, α, γ and ϵ, for the volume of 7.05 Å^3/atom, corresponding to the density of EIC, and for temperatures up to 5800 K by employing the same self-consistent in the charge density full-potential DFT+DMFT framework as in the studies of ϵ-Fe described in the previous section. This work evaluated the impact of many-electron effects on the electronic structure, magnetic susceptibil-

ity and relative stability of the three Fe phases. All DFT+DMFT calculations were done for the corresponding perfect fixed lattices. The lattice vibrations play a paramount role at the extreme temperatures inside the EIC, but including their effect within a kind of DFT+DMFT-based molecular dynamics is prohibitively costly at present. The fixed-lattice calculations of Ref. [63], however, allowed evaluating the structural dependence of correlation effects, assessing (though quite roughly) their impact on the electronic free energy "landscape" in the structural coordinates. Subsequent works [89, 49] carried out similar calculations for Fe-rich FeNi alloys in order to assess the impact of Ni substitution on many-electron effects. A later study of Ref. [90] concentrated on the ϵ-phase evaluating its electronic state as well as electrical and thermal conductivities. The results obtained in these works for the electronic structure, magnetism, thermodynamic stability and transport are reviewed below.

3.1 Electronic structure and magnetic susceptibility of iron and iron-nickel alloys

The ratio Γ/T (see eq. 1) calculated at the EIC atomic volume as a function of T in Ref. [63] is shown in Fig. 6 for all relevant irreducible representations of the three phases. One may readily notice a qualitative difference in the behavior of Γ between these phases. The temperature scaling $\Gamma/T \propto T$ expected in the case of a good FL is clearly observed for the ϵ-phase. In contrast, Γ/T for the bcc iron e_g states features a linear and steep rise for $T < 1000$ K and then behaves non-linearly, indicating a non-coherent nature of those states at high temperatures. The bcc Fe t_{2g} and fcc Fe e_g electrons are in an intermediate situation with some noticeable deviations from the FL behavior.

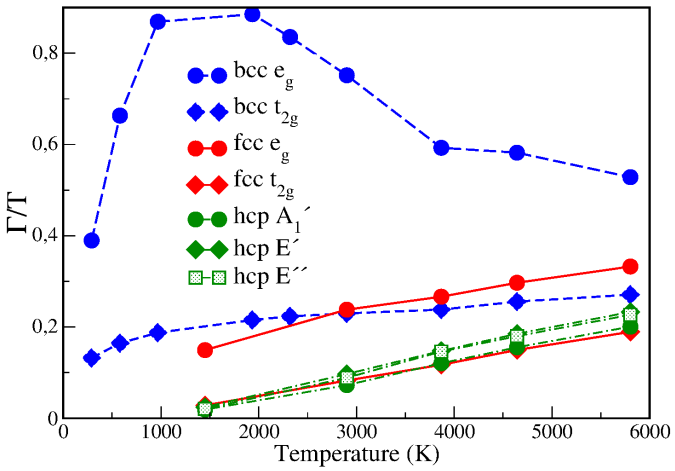

Figure 6: The ratio of the inverse quasiparticle lifetime Γ to temperature T vs. T. The solid red, dashed blue and dash-dotted green curves correspond to 3d states in fcc, bcc, and hcp Fe, respectively. They are split by the crystal field into t_{2g} (diamonds) and e_g (circles) representations in the cubic (bcc and fcc) phases, and two doubly-degenerate (E' and E'', shown by diamonds and squares, respectively) and one singlet (A_1', circles) representations in the hcp phase, respectively . A non-linear behavior of Γ/T for bcc Fe e_g states is clearly seen. Adapted from Ref. [63].

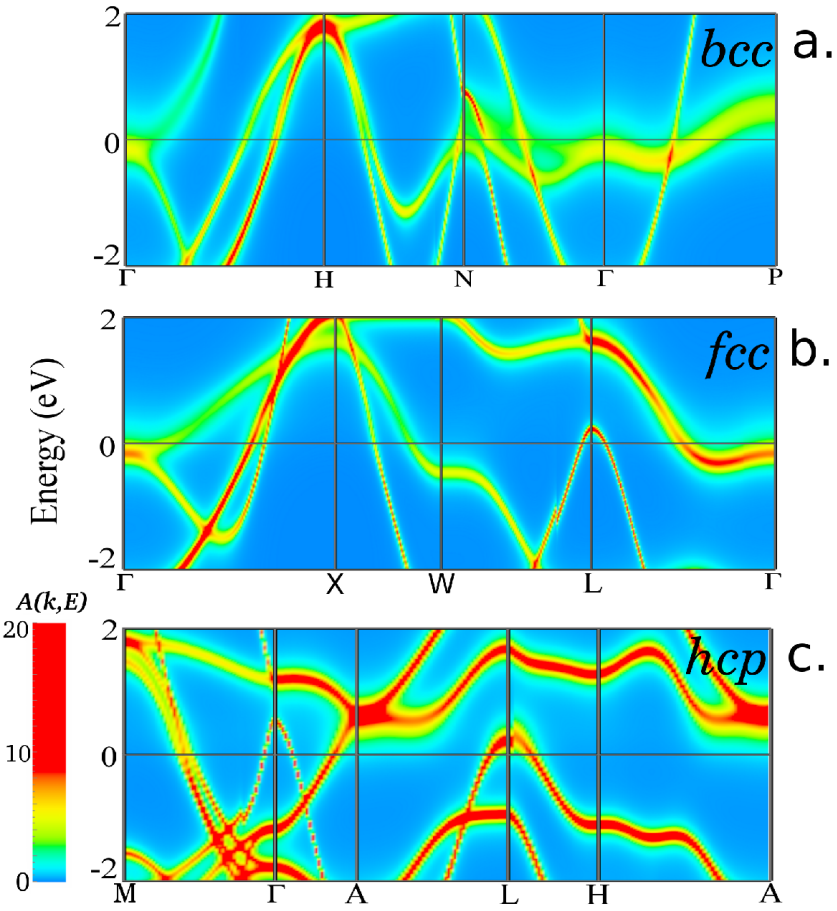

Figure 7: The DFT+DMFT **k**-resolved spectral function $A(\mathbf{k},\omega)$ (in V_{atom}/eV) for bcc (a), fcc (b), and hcp (c) Fe at volume V_{at} =7.05 Å^3/atom and temperature 5800 K. A non-quasiparticle e_g band is seen in the vicinity of the Fermy energy along the $N-\Gamma-P$ path in (a). Adapted from Ref. [63].

The same conclusions can be drawn from the **k**-resolved spectral function $A(\mathbf{k},\omega)$ plotted in Fig. 7 for the temperature of 5800 K. The bcc phase features a low-energy e_g band along the $N-\Gamma-P$ path that is strongly broadened, thus indicating destruction of quasiparticle states. The nFL behavior of e_g states in α-Fe is explained by the narrow peak in its partial density of states (PDOS) induced by a van Hove singularity in the vicinity of E_F. Such narrow peak in PDOS located at E_F leads to suppression of the low-energy hopping and to the corresponding enhancement of correlations[91]. In hcp Fe the electronic states in the vicinity of E_F are sharp (their red color indicating high value of $A(\mathbf{k},\omega)$), hence $\epsilon-$Fe exhibits a typical behaviour of a FL with large quasi-particle life-times in the vicinity of E_F. γ-Fe is in an intermediate state, with some broadening noticeable in the e_g bands at E_F in the vicinity of the Γ and W points.

The conclusion of Ref. [63] on the FL nature of ϵ-Fe was subsequently challenged by Zhang *et al.* [92], who recalculated ϵ-Fe at the EIC volume within DFT+DMFT [2] and found a strongly

[2]Ref. [92] was subsequently retracted by the authors ([93]) due to a numerical mistake in their transport calculations. However, this retraction does not concern their conclusions on a nFL nature of ϵ-Fe at the EIC conditions.

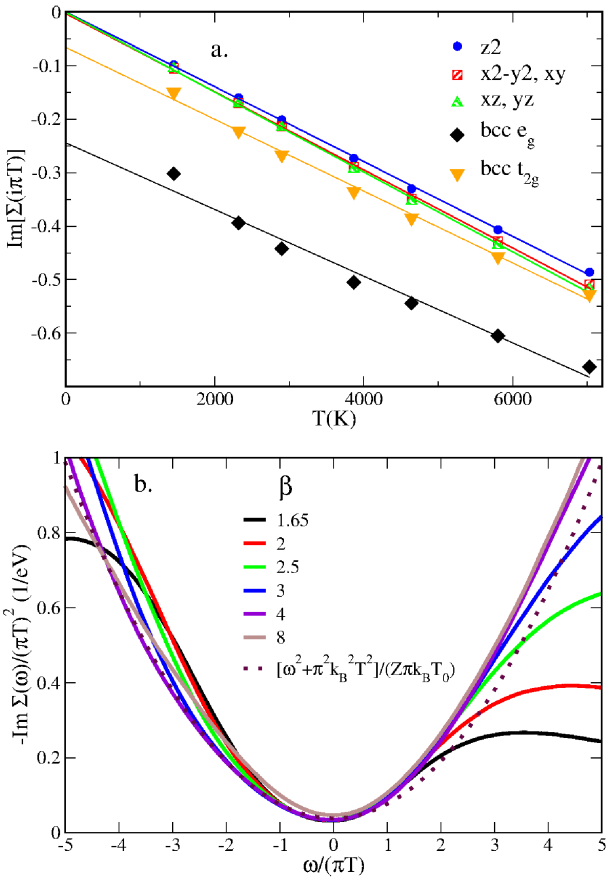

Figure 8: Fermi-liquid scaling of the DMFT self-energy in ϵ-Fe. a. The imaginary part of the DMFT self-energy at the first Matsubara point $\omega_1 = i\pi k_B T$ vs. temperature for hcp and bcc Fe. Note that $Im[\Sigma(i\pi k_B T)]$ being proportional to T is a signature of a Fermi-liquid [94] . The lines are the linear regression fits to the calculated points for corresponding $3d$ orbitals of Fe. b. The rescaled imaginary part of the DMFT self-energy at the real axis $Im[\Sigma(\omega)]/(\pi k_B T)^2$ vs. $\omega/(\pi k_B T)$. One sees that all self-energies collapse into a single curve described by a parabolic fit (the dotted line) defined by the quasiparticle weight Z =0.7 and the characteristic Fermi-liquid temperature scale T_0 =12 eV. Adapted from Ref. [90].

nFL linear dependence of Γ vs. T. In contrast to Ref. [63] employing the density-density approximation to the local Coulomb vertex defined by U =3.4 eV and J_H =0.94 eV, Zhang *et al.* used the full rotationally-invariant form for the vertex parametrized by a higher value of U = 5 eV and almost the same J_H. Therefore, in order to convincingly establish the nature of electronic state in ϵ-Fe Ref. [90] performed new DFT+DMFT calculations for the ϵ-phase with the full rotationally-invariant Coulomb interaction and explored the range of U from 4 to 6 eV. These calculations predicted an almost perfectly quadratic FL temperature scaling of Γ.

A significant problem in the analysis of DFT+DMFT results carried out in Refs. [63, 92] stems from the fact that the DMFT self-energy is calculated by CT-QMC on imaginary-frequency Matsubara points. The analytical continuation needed to obtain real-frequency data from this imaginary-frequency self-energy $\Sigma(i\omega)$ is known to be a mathematically ill-defined problem and quite sensitive to the details of its implementation. Even the extrapolation of $\Sigma(i\omega)$ to ω =0

needed to evaluate Γ, eq. 1, becomes rather less reliable for high temperatures, where the first Matsubara point $\omega_1 = i\pi k_B T$ is significantly shifted away from the real axis.

Hence, Ref. [90] also assessed the FL nature of ϵ-Fe by analyzing the imaginary-frequency self-energy without resorting to any analytical continuation. This is done by employing the so-called "first-Matsubara-frequency" rule. As demonstrated, e. g., by Chubukov and Maslov [94], in a Fermi liquid the imaginary part of electronic self-energy at the first Matsubara point within a local approximation like DMFT must be proportional to the temperature, i.e. $Im[\Sigma(i\pi k_B T)] = \lambda T$, where λ is a real constant. In Fig. 8a $Im[\Sigma(i\pi k_B T)]$ is plotted as a function of temperature for all inequivalent orbitals in hcp and bcc Fe. One clearly sees that in the ϵ phase $Im[\Sigma(i\pi k_B T)]$ is almost perfectly proportional to T, in contrast to bcc Fe, where it exhibits significant deviations from the "first-Matsubara-frequency" rule. This deviation is especially pronounced for the e_g states of the bcc phase, which are indeed of a strongly nFL nature, as discussed above.

Pourovskii *et al.* [90] also verified the scaling of the full analytically-continued DMFT self-energy , which in a FL state exhibits the quadratic frequency dependence at low ω with $\Sigma(\omega) = C \cdot (\omega^2 + (\pi k_B T)^2)$. The constant of proportionality C can be written as $1/(Z\pi k_B T_0)$ with the characteristic scale $T_0 \sim 10 T_{FL}$, where T_{FL} is the temperature where resistivity ceases to follow a strict T^2 temperature dependence [95]. Indeed, one sees in Fig. 8b that the real-frequency self-energies for different temperatures collapse into a single curve when plotted as $Im[\Sigma(\omega)]/(\pi k_B T)^2$ vs. $\omega/(\pi k_B T)$. The value of $k_B T_0 = 12$ eV extracted from this plot corresponds to a T_{FL} ≈14000 K, which is significantly higher than the range of temperatures expected inside the EIC. This analysis of both the Matsubara and real-ferquency self energy of ϵ-Fe has thus confirmed its FL state. We will see in Sec. 3.2 that this results has a direct bearing on the transport properties of ϵ-Fe at the EIC conditions.

The temperature dependence of uniform susceptibility $\chi(T)$ was also calculated by Ref. [63] by evaluating the response to a small external field. The obtained temperature dependence (see Fig. 9) is consistent with the results on electronic structure discussed above. A Pauli behavior found for the FL ϵ and γ phases, while the nFL bcc α exhibits a Curie-Weiss behavior well described by the fit $\chi = \frac{1}{3}\frac{\mu_{eff}^2}{T+\Theta}$ with μ_{eff} =2.6 μ_B and Θ =1396 K (see inset in Fig. 9). Alternatively, one may try to account for the same dependence with an enhanced Pauli law, $\chi = \chi_0/(1 - I * \chi_0)$, where I is the Stoner parameter and χ_0 is the bare susceptibility of Kohn-Sham band structure; the strong temperature dependence of χ is then caused by a narrow peak at E_F in the e_g PDOS due to the van Hove singularity. However, the enhanced Pauli-law fit describes $\chi(T)$ less well than the Curie-Weiss one, the difference is clear for lower T <3 below 2500 K. Hence, from these calculations one may infer the existence of a rather large local magnetic moment in the bcc phase at the EIC conditions. One may expect a significant contribution to the α-phase free energy due to the corresponding magnetic entropy.

Ruban *et al.* [96] also studied the stability of local moments in iron at the EIC atomic volume using a longitudinal spin-fluctuation model employing first-principles intersite exchange interactions. They predicted a local moment of approximately the same magnitude to be stable in all three phases at the EIC temperature of 6000 K and also obtained an evolution of χ vs. T that is qualitatively similar to the one of Ref. [63]. They explained the qualitative difference in $\chi(T)$

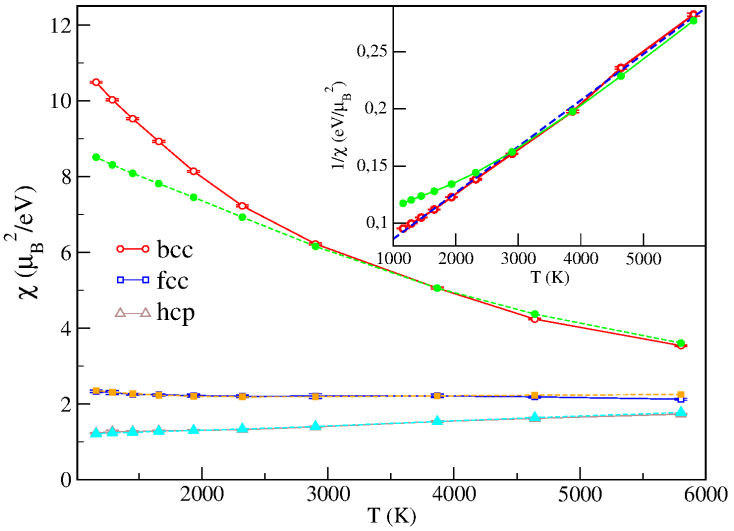

Figure 9: The uniform magnetic susceptibility in paramagnetic state versus temperature. The error bars are due to the CT-QMC stochastic error. The dashed lines with corresponding filled symbols are fits to the enhanced Pauli law, see the text. Inset: the inverse uniform magnetic suscptibility of bcc Fe is shown in red (empty circles), the blue dot-dashed and green (filled circles) lines are fits to the Curie-Weiss and enhanced Pauli law, respectively. Adapted from Ref. [63].

between the three phases by an impact of pair interactions. Vekilova *et al.* [89] has subsequently studied the DMFT local susceptibility χ_{loc} , i. e., the response to a local field applied to a single iron site, vs. T. They found a Curie-like temperature evolution in the bcc phase and a Pauli-like quasi temperature independent χ_{loc} in hcp-Fe. One may notice that within the single-site DMFT approximation χ_{loc} cannot be affected by intersite interactions. Hence, a qualitatively different behavior of χ_{loc} in the three phases hints at the key role of local correlation effects, in particular, existence of a local moment in bcc-Fe and its absence in the hcp phase.

The EIC is expected to contain, apart of iron, also non-negligible contributions of other transition metals, mainly of nickel as evidenced by the composition of metallic meteorites. The contribution of nickel is evaluated to 5-10% based on geochemical models [97]. The impact of Ni substitution on many-electron effects in iron at the EIC conditions is hence an important subject and has been studied by [89, 49]. In particular, Vekilova *et al.* [89] employed the same computational framework as Ref. [63] and modeled the random Fe_3Ni alloy by the smallest supercells capable to accommodate 25% of Ni substitution. These supercells comprise two, one, and two conventional cells in the case of bcc, fcc, and hcp lattices, respectively. In order to model more realistic lower Ni concentrations one would have to employ larger supercells with the corresponding heavy increase in the computational effort. In addition, Vekilova *et al.* made use of different environment of two inequivalent Fe sites in their bcc and hcp supercells , with only one of those having Ni nearest neighbors, to evaluate the effect of Ni nearest neighbors on correlations on iron sites. Many-electron effects on Ni were included in the same way as for Fe with the corresponding local Coulomb interaction specified by the same values of $U = 3.4$ eV and J_H =0.9 eV.

The effect of Ni nearest neighbors (NN) on electronic correlations on Fe sites was found to be

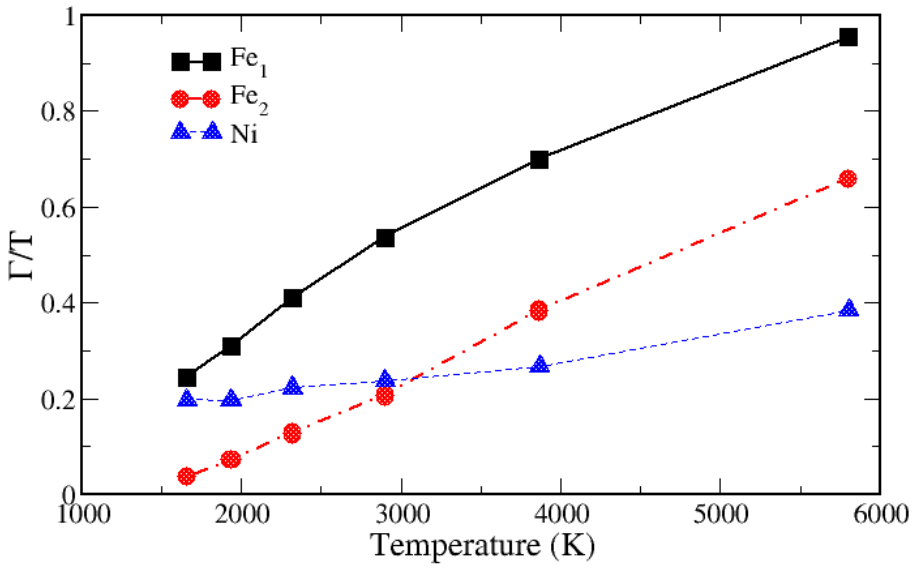

Figure 10: The inverse quasiparticle lifetime Γ as a function of T for three inequivalent sites, Fe_1 (six Ni and six Fe nearest neighbors) , Fe_2 (all nearest neighbors are Fe) and Ni, in the hcp Fe_3Ni supercell.

structure-dependent. In the bcc phase it results in significant deviations from the Curie-Weiss behavior for the uniform susceptibility χ and reduced Γ for the e_g states. Overall the presence of Ni NNs reduced the degree of "non-Fermi-liquidness" for the bcc e_g states. The opposite effect was found for the hcp phase, where the presence of Ni NNs enhanced the uniform susceptibility and Γ (Fig. 10). These effects can be related to modifications of corresponding Fe PDOS due to the presence of Ni NNs. Namely, in the case of bcc one observes a smearing of the e_g peak at E_F, conversely, in the case of ϵ-Fe a characteristic dip in PDOS in the vicinity of E_F becomes more shallow.

Vekilova *et al.* found rather weak correlation effects on Ni sites at the EIC conditions. As shown in Fig. 10, Γ for Ni features a nFL behavior with a rather slow increase in the studied range of T.

Many-electron effects in Ni and FeNi alloys under extreme conditions were subsequently studied in a recent work by Hausoel *et al.* [49]. The authors employed a DFT+DMFT technique that is similar to the one used in Refs. [63, 89] and mainly focused on nFL properties of Ni t_{2g} states, this question was not addressed by the previous works. They modeled random $Fe_{1-x}Ni_x$ alloys (x =0.05, 0.20) at the EIC density within the coherent-potential approximation (CPA). The advantage of CPA is that one can treat any concentration x with the same computational cost, however, the local environment effects, which seems to be quite important as one sees in Fig. 10, are neglected. Hausoel *et al.* predicted a strong enhancement of Γ due to the Ni substitution as compared to pure ϵ-Fe for the studied range of temperatures up to 2000 K. This result is in agreement with Fig. 10, if one compares the magnitude of Γ for the iron site Fe_2 without Ni NNs with that for Ni at T <2000 K. However, one also sees that Γ of Ni exhibits a slow almost linear-in-T scaling, while Γ of Fe_2 scales quadratically with T, hence at the EIC temperature of

about 6000 K the scattering due to the iron sites dominates and the Ni contribution is relatively weaker.

3.2 Electron-electron scattering and transport in ϵ-Fe

Transport properties of iron at the extreme conditions are of significant importance for geophysics. In particular, the thermal conductivity of the iron-rich matter inside the liquid outer core of Earth is a key parameter determining the stability of the geodynamo generating the Earth's magnetic field. This geodynamo runs on heat from the growing solid inner core and on chemical convection provided by light elements issued from the liquid outer core on solidification [78]. The power supplied to drive the geodynamo is proportional to the rate of inner core growth, which in turn is controlled by heat flow at the core-mantle boundary [98]. This heat flow critically depends on the thermal conductivity of liquid iron under the extreme pressure and temperature conditions in the Earth's core. For a long time there has been agreement that convection in the liquid outer core provides most of the energy for the geodynamo since at least 3.4 billion years [99, 100]. Recently, such a view has been challenged by first-principles calculations [101, 78], suggesting a much higher capacity for the liquid core to transport heat by conduction and therefore less ability to transport heat by convection [99]. The calculated conductivities have been found to be two to three times higher than the earlier generally accepted estimates.

Convection also plays a crucial role in the current theory of the EIC dynamics, as a radial motion of the inner core matter is invoked to explain the observed seismic anisotropies of the inner core [102, 103, 104]. However, *ab initio* calculations of Ref. [105] similarly predict a too high thermal conductivity for hexagonal close-packed (hcp) ϵ-iron to sustain this convection.

These first-principles calculations for liquid and solid iron [101, 78, 105] employed the standard density-functional-theory (DFT) framework in which electron-electron repulsion is not properly accounted for as dynamical many-body effects are neglected. Hence, the contribution to resistivity from the electron-electron scattering (EES) of d-electrons due to correlations was not taken into account in those calculations. In order to elucidate how large the EES contribution to the electrical and thermal resistivity at Earth's core conditions Ref. [90] extended their DFT+DMFT approach to calculations of the electrical and thermal conductivities of pure ϵ-Fe at the EIC density. Using the analytically-continued DMFT self-energy (see Fig. 8b) they evaluated the conductivity from the corresponding DFT+DMFT spectral function using the Kubo linear-response formalism[106, 107]. Namely, the electrical and thermal conductivity read

$$\sigma_{\alpha\alpha'} = \frac{e^2}{k_B T} K^0_{\alpha\alpha'}, \tag{2}$$

$$\kappa_{\alpha\alpha'} = k_B \left[K^2_{\alpha\alpha'} - \frac{(K^1_{\alpha\alpha'})^2}{K^0_{\alpha\alpha'}} \right], \tag{3}$$

where α is the direction (x, y, or z), k_B is the Boltzmann constant. The kinetic coefficients $K^n_{\alpha\alpha'}$ can be calculated from the real-energy DFT+DMFT spectral function $A(\mathbf{k}, \omega)$ and the velocities of Kohn-Sham states, $v_\alpha(\mathbf{k})$, the later is evaluated by DFT band structure methods as described, e. g., Ambrosch-Draxl *et al.* [108] for the case of LAPW method.

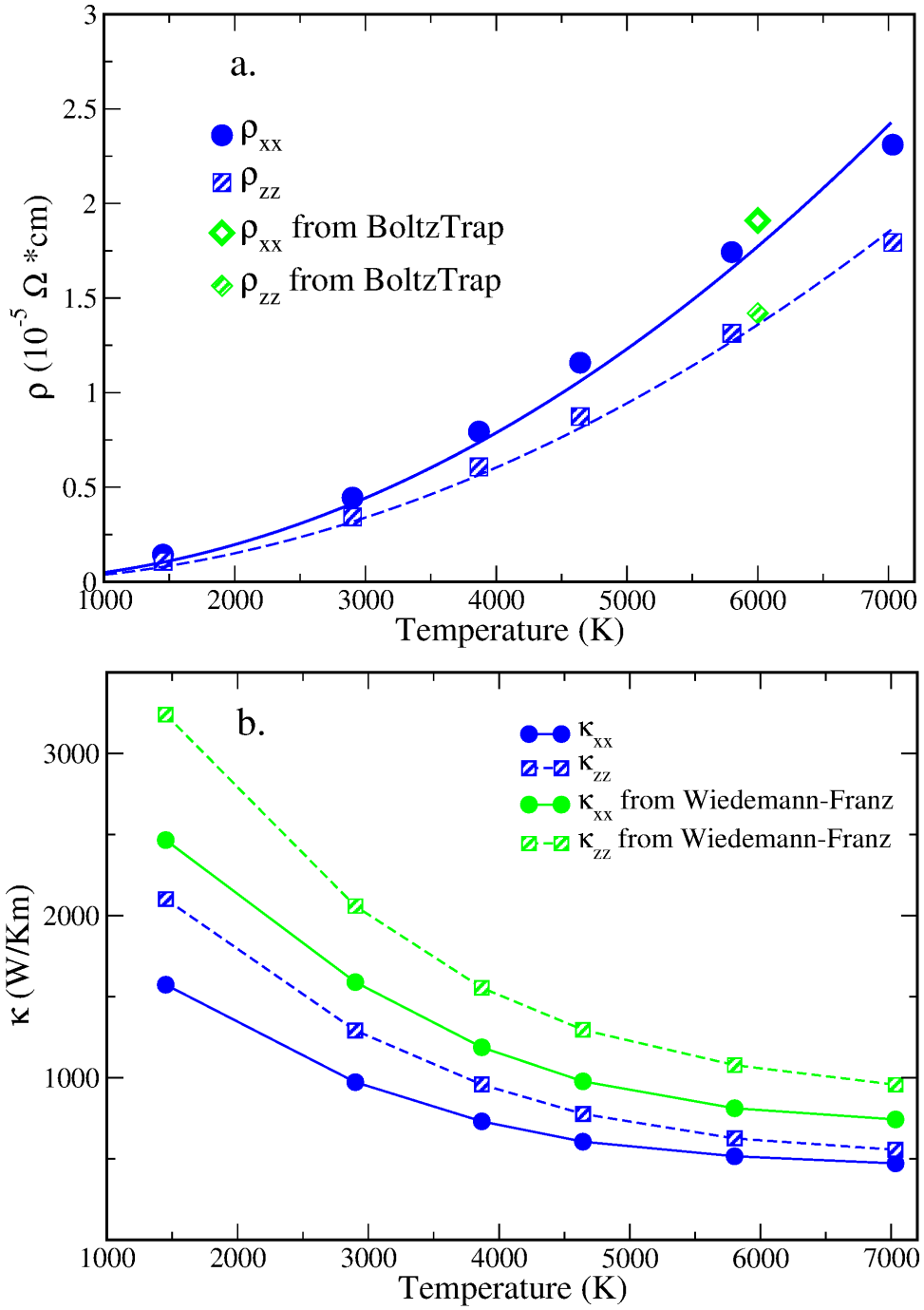

Figure 11: Calculated electron-electron-scattering contribution to the electrical and thermal resistivity of hcp iron at Earth's core density. a. Electrical resistivity. Blue filled circles and hashed squares are DFT+DMFT results for ρ_{xx} and ρ_{zz} , respectively. Green empty and hashed diamonds are the corresponding resistivities calculated by the Boltzmann-transport code BoltzTrap [109] assuming a Fermi-liquid with the scattering rate Γ/Z =0.09 eV. b. Thermal conductivity. Blue filled circles and hashed squares are DFT+DMFT results for κ_{xx} and κ_{zz}, respectively. Green lines/symbols are the corresponding conductivities obtained from the calculated electrical conductivity using the Wiedemann-Franz law with the standard Lorenz number of $2.44{\cdot}10^{-8}$ WΩK^{-2}. Adapted from Ref. [90].

The contributions of electron-electron scattering into the electrical resistivity and thermal conductivity of ϵ-Fe obtained by Ref. [90] are displayed as a function of T in Figs. 11a and 11b, respectively. First, one sees that the electrical resistivity ρ features a clear T^2 FL dependence, as expected on the basis of the analysis of its DMFT self-energy as discussed in Sec. 3.1. Second, its magnitude of $1.6\cdot\ 10^{-5}$ Ω·cm at T =5800 K is rather insignificant compared to the electron-phonon-scattering contribution of about $5.3{\cdot}10^{-5}$ Ω·cm predicted by DFT calculations of Pozzo *et al.* [105]. This indicates that the electron-electron scattering should not strongly influence the electrical resistivity in hcp-Fe at EIC conditions. Third, the electron-electron-scattering thermal conductivity κ_{e-e} of 540 $\mathrm{Wm^{-1}K^{-1}}$ T =5800 K is not high and comparable to the corresponding value due to the electron-phonon scattering κ_{e-ph} ≈300 $\mathrm{Wm^{-1}K^{-1}}$ obtained by Ref. [105]. Hence, in contrast to ρ the electron-electron scattering contribution to the thermal conductivity is quite important. By including both the electron-electron and electron-phonon scattering effects the total conductivity is reduced to about 190 $\mathrm{Wm^{-1}K^{-1}}$, hence, the corresponding resistivity is enhanced by about 60%.

An important observation of Ref. [90] is that the DFT+DMFT electron-electron-scattering thermal conductivity of ϵ-Fe is significantly lower than the one calculated from the corresponding contribution to $\rho = 1/\sigma$ in accordance with the Wiedemann-Franz law, $\kappa/(\sigma T) = \frac{\pi^2}{3}\left(\frac{k_B}{e}\right)^2 = L_0$ (where the standard Lorenz number L_0 is $2.44{\cdot}10^{-8}\mathrm{W\Omega K^{-2}}$), see Fig. 11b. By employing simple analytical calculations in the Boltzmann formalism Herring [110] showed that the quadratic FL frequency dependence of the imaginary part of the self-energy and, hence, of the quasiparticle life-time

$$1/\tau(\epsilon) = 1/\tau(\epsilon = 0) \cdot \left(1 + \epsilon^2/(\pi k_B T)^2\right),$$

leads to a substantial reduction of the Lorenz number

$$\kappa/(\sigma T) = L_0/1.54 = L_{FL}.$$

The stronger effect of the frequency-dependence of $\tau(\omega)$ on the thermal conductivity as compared to σ is due to the additional power ϵ^2 in the numerator of the transport integrals for κ, see, for example, Ref. [111]. Hence, the enhancement of the electron-electron-scattering contribution to the thermal resistivity obtained within DFT+DMFT stems directly from the Fermi-liquid state of the ϵ-Fe phase at the EIC conditions. A similar reduction of the Lorenz number has been very recently obtained by another DFT+DMFT study [112]; the electron-electron contribution to the thermal conductivity of ϵ-Fe at the EIC conditions reported in this works is close to that of Ref. [90].

The reduction of the thermal conductivity due to the electron-electron scattering predicted by Ref. [90] is still insufficient to explain the stability of convection by itself. On the other hand, the extremely low values of κ_{tot} ∼50 $\mathrm{Wm^{-1}K^{-1}}$ may not be required to reconcile theoretical calculations of the thermal conductivity with geophysical observations [113, 114].

Moreover, the impact of alloying and lattice vibrations have not been to date taken into account in the DFT+DMFT transport calculations. For example, the DFT+DMFT calculations for Fe-Ni alloy at the inner core conditions discussed in the previous section point out an important local environment effects that may affect the electron-electron scattering in real material of the EIC. The impact of all those effects on transport properties of the EIC matter remains to be evaluated.

3.3 Many-electron effects and structural stability

The stable phase of pure iron at the EIC conditions has not been clearly identified experimentally; neither have *ab initio* DFT calculations resulted in an unambiguous prediction due to a small energy difference between the three phases, as described in the introduction of Sec. 3. Hence, corrections due to the many-electron effects neglected by DFT can have a qualitative impact on the nature of stable iron phase at the EIC conditions.

A quantitative estimation for the contribution of correlations to the electronic free energy of the three phases was obtained by Ref. [63] together with their other magnetic and electronic properties (see Sec. 3.1). Their fixed-lattice calculations neglected the contribution of lattice vibrations to the phase stability, which are expected to be very significant at such extreme temperatures. However, such calculations are still able to assess the structural dependence of this contribution.

In spite of the simplifying fixed-lattice approximation evaluating the electronic free energy within the DFT+DMFT framework remains a highly non-trivial task. The total-energy calculations in this framework have nowadays become quite standard as described in Sec. A.3. Such DFT+DMFT calculations evaluating the total energy using eq. 18 have been applied, for example, by Leonov *el al.* [41] to study the α-γ phase transition in iron.

In contrast, the partition function and, correspondingly, the DFT+DMFT grand potential (17) cannot be generally directly sampled by the usual Metropolis algorithm. In the context of DMFT quantum impurity problem solved by CT-QMC or other numerical technique, it is the contribution of DMFT functional $\Phi_{imp}[G_{loc}(\mathbf{R})]$ into (17), which is the sum of all local skeleton diagrams constructed with the local GF $G_{loc}(i\omega_n)$ and the on-site vertex, that cannot be computed directly. Different types of the numerical thermodynamic integration are employed instead, in particular, the one from an analytical high-temperature limit [115]. Such integration remains non-trivial in the present case of Fe at the EIC conditions, as the temperature $T \approx$6000 K is still low compared to other energy scales like the bandwidth or U. Ref. [63] employed instead the numerical thermodynamic integration over the coupling strength $\lambda \in [0:1]$, where the corresponding free energy is defined $F_\lambda = -\frac{1}{\beta} \ln \mathrm{Tr} \left(\exp[-\beta(\hat{H}_0 + \lambda \hat{H}_{int})] \right)$, H_0 is the one-electron part of the DFT+U Hamiltonian (5), $\hat{H}_{int} = \hat{H}_U - E_{DC}$ is the interacting part. The coupling constant integration results in the following expression for the many-body correction:

$$\Delta F = F - F_{DFT} = \int_0^1 \frac{\langle \lambda \hat{H}_{int} \rangle_\lambda}{\lambda} d\lambda, \tag{4}$$

where F_{DFT} is the electronic free energy in DFT. In derivation of Eq. 4 one neglects the λ dependence of the one-electron part, and, hence, the charge density renormalization due to many-body effects. In practice, the integrand in (4) was evaluated numerically with $\frac{\langle \lambda \hat{H}_{int} \rangle_\lambda}{\lambda}$ computed for a discrete mesh in $\lambda \in [0:1]$ by performing DFT+DMFT simulations with the Coulomb interaction scaled accordingly. This method was subsequently applied in DFT+DMFT calculations of Bieder *et al.* [116] to evaluate the free energy of the cerium metal.

The resulting DMFT correction to the free energy for the three iron phases is plotted in Fig. 12 togehter with the correction to the total energy calculated given by the difference of (18) and E_{DFT}. Within rather significant error bars the magnitude of ΔF is the same for bcc and hcp Fe,

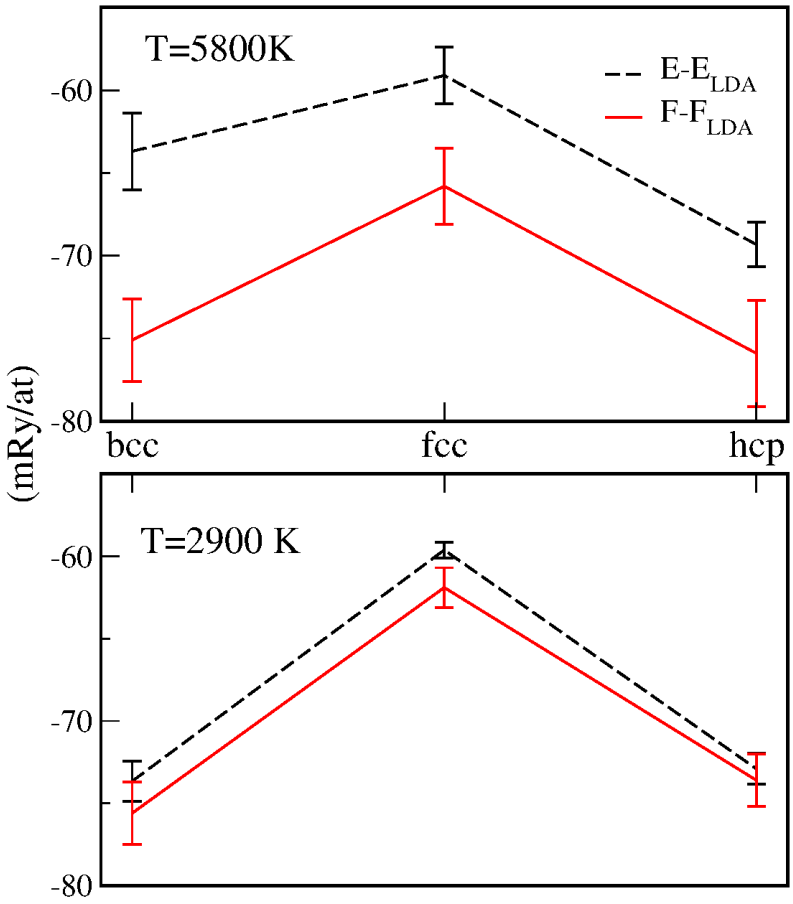

Figure 12: Many-body correction to the total (black dashed line) and free (red solid line) energy for the three phases of Fe at the volume of 7.05 Å/atom at T=5800 K (upper panel) and 2900 K (lower panel). The error bars are due to the CT-QMC stochastic error. Adapted from Ref. [63].

which are suggested as stable phases of iron [86] and iron-based alloys [117, 82] at the Earth's inner core conditions. Though the correlation strength (as measured, for example, by the inverse quasiparticle lifetime Γ, Fig. 6), is higher for α-Fe, this is apparently compensated by a higher value of U predicted for the ϵ-phase by cRPA calculations of the same work [63]. The magnitude of ΔF is, however, at least several mRy smaller in the case of fcc Fe, showing that the many-body correction may significantly affect relative energy differences among iron phases at the Earth core conditions. One may also notice that the entropic contribution $T\Delta S = \Delta E - \Delta F$ becomes much more significant at the higher temperature, and its contribution is almost twice larger in the case of the bcc phase compared with two others. This is in agreement with the local-moment behavior of this phase predicted by DFT+DMFT calculations, as described in Sec. 3.

4 Conclusions and perspectives

In this highlight we have reviewed recent *ab initio* studies of the role of many-electron effects in various phases of iron at extreme conditions. In particular, a significant enhancement of dynamical correlations at the pressure-induced $\alpha \rightarrow \epsilon$ phase transition is predicted by these

calculations. This enhancement is explained by the fact that dynamical correlations are strongly suppressed by the static spin polarization in ferromagnetic α-Fe; this polarization is absent in paramagnetic hcp ϵ-Fe. In result, DFT+DMFT calculations predict large many-body corrections to the equation of state of the ϵ-phase and a significant electron-electron scattering contribution to its electrical resistivity. The same theoretical framework predicts an electronic topological transition to occur in this intermediate pressure range thus explaining the observed peculiarities in the evolution of its hexagonal cell parameters, Debye velocity and Mössbauer central shift.

Applying the same framework to the geophysically-important regime of the Earth's inner core (EIC) conditions one finds a strong structural dependence for many-electron effects. Namely, bcc α-Fe exhibits a clearly non-Fermi liquid behavior as evidenced by a sub-linear temperature dependence of the quasiparticle scattering rate Γ and a Curie-Weiss-like behavior of the magnetic susceptibility. In contrast, an almost perfectly Fermi-liquid state is predicted for ϵ-Fe at the same EIC conditions, with sharp quasiparticle bands at low-energy and the T^2 scaling of Γ. The fcc γ phase is found to be in an intermediate regime between bcc and hcp with some noticeable deviations from Fermi-liquid state. The contribution of correlation effects to the electronic total and free energies is consequently also strongly structurally-dependent. The strength of many-electron effects on iron is found to be sensitive to the local environment and quite significantly affected by the presence of Ni nearest neighbors; our calculations also show comparatively weaker correlations on Ni sites themselves at the EIC conditions. Finally and quite unexpectedly, the predicted "dull" Fermi-liquid state of ϵ-Fe leads to a significant suppression of the Lorenz number with the corresponding enhanced contribution of the electron-electron scattering to the thermal resistivity. This enhancement of the thermal resistivity as compared to electrical one is directly related to a strong (quadratic) frequency dependence of the Fermi-liquid electron-electron scattering rate.

All these results have been obtained by the DFT+DMFT in conjunction with the numerically-exact continuous-time quantum Monte Carlo method, which is equally reliable for all considered regimes of correlations (e. g., Fermi-liquid/non-Fermi-liquid, paramagnetic/ferromagnetic states). However, this technique, as well as overall DFT+DMFT framework, is numerically heavy and some approximations had to be employed to make these calculations feasible:

- The calculation of Ref. [61] employed the single-site DMFT in conjunction with a density-density local vertex. Though these calculations successfully accounted for the ground-state properties of the ϵ phase, the electron-electron scattering contribution into the resistivity was apparently strongly underestimated. The non-density-density spin-flip terms of the local vertex were also found in this work to be essential to account for the collapse of static antiferromagnetism in this phase. The effect of rotationally-invariant interaction in ϵ-Fe thus needs to be fully investigated. A very significant contribution of the electron-electron scattering to the electrical resistivity of ϵ-Fe and its non-Fermi-liquid behavior at low temperatures, as well as the non-conventional (spin-fluctuation-pairing) superconductivity experimentally observed in this phase, hint at important inter-site correlations, which can be included only by approaches beyond the single-site approximation.

- The density-density approximation for the local vertex is most probably less severe in the case of EIC conditions. In particular, the inclusion of rotationally-invariant local

interaction the study of ϵ-Fe by Ref. [90] led only to some quantitative changes compared to the previous study within the density-density approximation. The non-local correlations are also expected to be less important away from magnetic instabilities and with a lower strength of correlations at the high-density of the EIC matter. In contrast, the fixed-lattice approximations is quite severe when one considers temperatures just below the melting. Correspondingly, future studies of the impact of lattice vibrations on electronic correlations and vice versa are in this case of high importance.

Hopefully, the recent progress in development of extended-DMFT frameworks, see Rohringer *et al.* [118] for a recent review, will eventually make accessible the most important two-particle quantities (e.g., the full $\mathbf{k}$ and ω-dependent susceptibility or the vertex correction to the transport) for realistic multi-band systems with possibly significant intersite correlation, like ϵ-Fe in the moderate pressure range.

Regarding the second point: though fully consistent DFT+DMFT *ab initio* molecular dynamics will remain prohibitively computationally expensive for some time, one may still make use of the usual approximation of evaluating the electronic structure at fixed ionic coordinates. Hence, in order to assess the effect of lattice distortions on many-electron effects one may employ a set of supercells representing characteristic deviations from the perfect atomic positions expected at the relevant temperature for a given phase. Conversely, the impact of electronic correlations on lattice vibrations, at least in the harmonic approximation, can be studied using the recently formulated DFT+DMFT schemes for calculation of forces and phonon dispersions [31, 119, 120]. Eventually, the impact of light elements inclusions needs to be also included in realistic simulations of the EIC matter.

Acknowledgments

This review is mainly based on several recent works [63, 64, 61, 89, 90] carried out by me with a number of coauthors. I want to especially acknowledge the valuable contribution of my colleagues theoreticians I. A. Abrikosov, A. Georges, J. Mravlje, and S. I. Simak. I am also grateful to other coauthors of these papers: M. Aichhorn, M. Ekholm, M. I. Katsnelson, T. Miyake, A. V. Ruban, F. Tasnádi, O. Vekilova, V. Vildosola as well as our experimental collaborators from the group of L. Dubrovinsky. The many-body approaches employed in these papers were provided by the software library "TRIQS" that has been developed over years by O. Parcollet, M. Ferrero and collaborators. I thank S. Biermann, M. Gabay, D. Givord, J. Kunes, M. Rozenberg, G. Sangiovanni, M. van Schilfgaarde for critical reading of this manuscript and useful comments. The support of ANR and DFG under the collaborative project "RE-MAP" as well as of the European Research Council Grant No. ERC-319286-QMAC is gratefully acknowledged.

Appendix

A *Ab initio* dynamical mean-field theory approach: an overview

The standard DFT framework is well known to be deficient in the case of partially-filled narrow bands; the effect of a local Coulomb repulsion on the physics of such states cannot be captured by local or semi-local exchange-correlation functionals like the local-density or generalized-gradient approximations. As discussed in the introduction section, the $3d$ band of iron, while having a bandwidth larger than the relevant local Coulomb interaction, still cannot be satisfactory captured within pure DFT.

The approach employed for ab initio studies discussed in this highlight is thus based on supplementing the quadratic Kohn-Sham (KS) Hamiltonian H_0 with explicit local Coulomb interaction between Fe $3d$ states, the resulting "DFT+U" Hamiltonian [15, 121] reads

$$\hat{H}_{DFT+U} = \hat{H}_0 + \hat{H}_U - E_{DC} = \sum_{\mathbf{k}\nu} \epsilon_{\mathbf{k}\nu} c^\dagger_{\mathbf{k}\nu} c_{\mathbf{k}\nu} + \sum_{\substack{i,\\1,2,3,4}} \langle 12|U|34\rangle d^\dagger_{i1} d^\dagger_{i2} d_{i4} d_{i3} - E_{DC}, \qquad (5)$$

where $c^\dagger_{\mathbf{k}\nu}(c_{\mathbf{k}\nu})$ is the creation(annihilation) operator for the Kohn-Sham state $\psi_{\mathbf{k}\nu}$ at k-point $\mathbf{k}$ and the band index ν, $d^\dagger_{i\alpha}(d_{i\alpha})$ is the operator creating (annihilating) localized states $w_{i\alpha}$ on the correlated ($3d$) shell[3] in the unit cell i, $\alpha \equiv 1, 2, ...$ is a compound index for relevant quantum numbers labeling one-electron orbitals within that shell (for example, $\alpha \equiv \{m\sigma\}$, where m is the orbital quantum number and σ is the spin). The last term, E_{DC}, is the double-counting correction, which will be discussed below.

The interacting term in the DFT+U Hamiltonian is naturally defined in the real space, as the interaction is assumed to act between orbitals localized on the same atomic site. A sufficient localization of the orbitals $w_{i\alpha}$ at the correlated site is thus necessary for the DFT+U Hamiltonain to be physically sensible. For extended orbitals the intersite interactions are comparable to U; neglecting them in (5) thus becomes a poor approximation [122, 123]. However, in solids one cannot define d or f orbital as in an isolated atom, as such definition makes sense near the nucleus, where the crystalline potential is approximately spherical, but not in the interstitial.

There exists a number of approaches for constructing such bases representing localized correlated states in solids. For example, one may employ a basis-independent framework [124, 125, 126, 127, 128] defining the localized orbitals $w_{i\alpha}$ as Wannier functions constructed from a subset $\mathcal{W}$ of Kohn-Sham bands:

$$w_{i\alpha}(\mathbf{r}) = \sum_{\mathbf{k}\in BZ} w_{\mathbf{k}\alpha}(\mathbf{r} + \mathbf{R}_i) e^{-i\mathbf{k}\mathbf{R}_i} = \sum_{\substack{\mathbf{k}\in BZ\\ v\in\mathcal{W}}} e^{-i\mathbf{k}\mathbf{R}_i} \psi_{\mathbf{k}\nu}(\mathbf{r} + \mathbf{R}_i) P_{\nu\alpha}(\mathbf{k}), \qquad (6)$$

where the subset $\mathcal{W}$ comprises KS bands with a substantial contribution due to correlated orbitals, $\mathbf{R}_i$ is the lattice vector of the unit cell i, $\hat{P}(\mathbf{k})$ is a complex matrix such that the resulting orbitals form an orthonormalized basis, $\langle w_{i\alpha}|w_{j\beta}\rangle = \delta_{ij}\delta_{\alpha\beta}$. In fact, matrices $\hat{P}(\mathbf{k})$ possessing such properties are well-known to be not uniquely defined, the resulting gauge freedom in $\hat{P}(\mathbf{k})$

[3] For simplicity here and below we consider the case of a single correlated site per unit cell

can be exploited to obtain a well-localized basis of Wannier functions. Direct minimization of the spread of $w_{i\alpha}$ in the real space is employed to construct the maximally-localized Wanniers basis [124]. Another, a projective construction of localized Wannier functions, avoiding the explicit spread minimization, was proposed by Amadon *et al.* [128] and implemented in conjunction with the linearized augmented planewave (LAPW) band structure method by Aichhorn *et al.* [129]. One may also mention a hybrid method of Refs. [130, 131], in which Wannier functions are constructed from outward solutions of the radial Schrödinger equation and their energy derivatives on a chosen grid of energies. Another approach [47] makes use of the fact that some DFT band structure techniques expand Kohn-Sham states $\psi_{\mathbf{k}\nu}$ in a basis containing, among others, suitable "atomic-like" functions for a given correlated shell; such functions are then employed as a correlated-subspace basis. The somewhat older method of Ref. [132] writes the whole Hamiltonian (5) using atomic-like basis functions instead of $\psi_{\mathbf{k}\nu}$ and employs a subset of them to represent correlated orbitals; this approach is applicable only for few band-structure techniques employing such suitable basis functions.

Once the basis of correlated orbitals $w_{i\alpha}$ is chosen one needs to determine the on-site Coulomb repulsion between them. In principle, one may easily evaluate matrix elements of the bare Coulomb interactions $u(\mathbf{r}) = 1/r$ between such orbitals. The bare Coulomb repulsion is, however, known to be a very poor approximation for the local interaction in solids in eq. 5. For example, the average over its matrix elements between Ni $3d$ orbitals in NiO evaluates to about $20-25$ eV [133]. Experimentally, though, one finds that the splitting between occupied and empty $3d$ localized features seen in the PES/inverse-PES spectra, which is, to a first approximation, the average $\langle U \rangle$, amounts only to about 9 eV [134][4]. This discrepancy is, of course, due to the fact that the on-site interaction between localized orbitals in solids is strongly screened by itinerant states. Hence, one should view the Hamiltonian (5) as a *low-energy* description of the correlated system, where the interactions between localized states $w_{i\alpha}$ and itinerant bands, which are not explicitly included, have been integrated out. In result, the effective Coulomb repulsion $u(\mathbf{r}, \mathbf{r}', \omega)$ acquires a frequency dependence, which is then passed to matrix elements in the correlated-orbitals basis:

$$\langle 12|U|34\rangle(\omega) = \int d\mathbf{r} d\mathbf{r}' w^*_{i1}(\mathbf{r}) w^*_{i2}(\mathbf{r}') u(\mathbf{r}, \mathbf{r}', \omega) w_{i3}(\mathbf{r}) w_{i4}(\mathbf{r}'), \tag{7}$$

with the low-frequency limit of $\langle 12|U|34\rangle(\omega)$ giving a value of on-site repulsion that is strongly reduced by screening; it is relevant for the low-energy physics described by (5). The high-frequency limit of $\langle 12|U|34\rangle(\omega)$ approaches the bare Coulomb value; this high-frequency tail of $\langle 12|U|34\rangle(\omega)$ may affect the low-energy physics producing an additional enhancement of quasiparticle renormalization [62]; it also induces high-energy plasmonic spectral features [135].

Due to this complex effect of screening the local Coulomb repulsion is rather difficult to evaluate from first principles and often treated as a parameter. A more consistent and truly *ab initio* approach is based on evaluating the screening of local repulsion between a given set of local orbitals $w_{i\alpha}$ from the Kohn-Sham band structure. One popular approach of this kind, the constrained random-phase approximation (cRPA) [136], separates the polarization function $\Pi(\omega) = \Pi_c(\omega) + \Pi_r(\omega)$ evaluated within RPA into the contribution $\Pi_c(\omega)$ due to transitions

[4]The optical gap of about 4 eV in this compounds is of the charge-transfer (O $2p \rightarrow$ Ni $3d$) type.

within the subset of correlated bands $\mathcal{W}$ and $\Pi_r(\omega)$ due to all other transitions. Then the relevant interaction is obtained by screening the bare Coulomb repulsion $v(\mathbf{r})$ with Π_r and then projecting $u(\mathbf{r}, \mathbf{r}', \omega)$ into the subspace of $w_{i\alpha}$ using (7). The cRPA method is a powerful technique that is able to obtain all matrix elements of $\langle 12|U|34\rangle(\omega)$ with their frequency dependence. However, cRPA is not particularly well suited for the case of a significant entanglement between the correlated $\mathcal{W}$ and itinerant band subspaces, which is precisely the case in $3d$ transition metals, where the dispersive $4s$ band crosses and mixes with the narrow $3d$ one. It is difficult to define a consistent separation of the polarization into $\Pi_c(\omega)$ and $\Pi_r(\omega)$ in this case, though some versions of cRPA to handle this entanglement have been formulated [19, 137].

An alternative approach to first-principles evaluation of the local interaction is based on the assumption that a quantitatively correct static screening of the on-site interaction is already included at the DFT level through the local XC potential. This approach named constrained LDA (cLDA) [138, 139, 16] constrains the charge on the localized shell of interest on a single site within a supercell with other states unconstrained, hence, allowed to screen the on-site interaction. The band energy of corresponding "constrained" KS states is then evaluated as a function of its orbital occupancy allowing to extract the direct Coulomb repulsion parameter U and Hund's rule coupling J_H. The method was shown to provide reasonable values of the static interaction for pure iron [16, 17], though it is not free from uncertainties.

The Kohn-Sham band structure, which is the quadratic part of the DFT+U Hamiltonian (5), is that of non-interacting electrons moving in an effective potential. However, this potential contains, among other terms, the Hartree and XC potentials corresponding to the electron density of the Kohn-Sham states. Hence, the Kohn-Sham bands are not truly those of a non-interacting system. In particular, the effect of the screened Coulomb interaction $u(\mathbf{r}, \mathbf{r}', \omega)$ acting between correlated orbitals is included in a static mean-field way by LDA; this fact is used by the cLDA method described above to extract the value of this interaction. As the same interaction explicitly enters into (5), it is necessary to remove this static mean-field contribution from the same Hamiltonain to avoid counting it twice. Hence, the corresponding double-counting correction (DC) is included as the last term into (5).

Though the local screened interaction is certainly included in some form by XC potentials determining its exact contribution is a highly nontrivial problem. Local and semi-local XC potentials are functions of the full charge density and also non-linear; they cannot be represented as a superposition of contribution due to different orbitals. Hence, the problem of formulating a theoretically sound expression for the DC term has not been fully solved to date. There exist a number of different DC formulae [15, 140, 45, 141, 142]. The most widely used ones are derived by assuming that XC potentials include the local Coulomb interaction in an orbitally-independent form. That form is given by the Hartree-Fock potential due to the on-site interaction term in (5) for a particular limit of the correlated-shell occupancy matrix. It is assumed to be uniform within the "around-mean-field" (AMF) approach [15], which is usually employed for weakly and moderately-correlated metals, e. g., in the case of iron. The alternative "fully-localized-limit' (FLL) form [140] assumes the most non-uniform occupancy matrix for a given shell filling and is generally employed for strongly-correlated systems like Mott insulators. The contribution due

to this term into the one-electron potential for a given orbital α is given by

$$\Sigma^{\alpha}_{DC} = \frac{\partial E_{DC}}{\partial \rho_{\alpha}}|_{\hat{\rho}_{DC}}, \tag{8}$$

where the derivative over the orbital occupancy ρ_{α} is taken at the shell's occupancy matrix $\hat{\rho}_{DC}$ corresponding to a given limit (AMF, FLL, etc.).

A.1 Dynamical mean-field theory

Once all terms in the Hamiltonian (5) are determined the next step is, obviously, solving it to obtain the ground-state and excited properties of a given real system. This represents a formidable problem, as one may notice that this Hamiltonian can be viewed as a multi-band generalization of the famous one-band Hubbard model (HM) for which no exact solution is known for the relevant 2d and 3d cases. A breakthrough in the study of HM was achieved in the beginning of 90th in the framework of dynamical mean-field theory (DMFT) [143, 144, 145]. Though initially the DMFT formalism was written for the one-band HM, here we present its formulation for the Hamiltonian (5) in view of applications to realistic materials. The DMFT framework focuses on the one-electron Green's function (GF) defined in the Kohn-Sham space and imaginary-time domain[5] as $G_{\nu\nu'}(\mathbf{k}, \tau - \tau') = -\langle \mathrm{T}[c_{\mathbf{k}\nu}(\tau)c^{\dagger}_{\mathbf{k}\nu'}(\tau')]\rangle$, where T is the time-ordering operator. Its Fourier transform $G(\mathbf{k}, i\omega_n)$ is the GF in the imaginary-frequency domain, where $i\omega_n = i\pi(2n-1)T$ is the fermionic Matsubara grid for the temperature T. Correlation effects arising due to the interaction U term of (5) are encoded in the Kohn-Sham space by the electronic self-energy $\Sigma^{KS}(\mathbf{k}, i\omega_n) = \hat{P}^{\dagger}(\mathbf{k})\Sigma(\mathbf{k}, i\omega_n)\hat{P}(\mathbf{k})$, where $\hat{P}(\mathbf{k})$ are projector matrices (6) to the correlated subspace, $\Sigma(\mathbf{k}, i\omega_n)$ is the self energy in that subspace spanned by the localized orbitals (6). The interacting lattice GF is thus obtained by inserting $\Sigma(\mathbf{k}, i\omega_n)$ through the Dyson equation:

$$G^{-1}(\mathbf{k}, i\omega_n) = G^{-1}_0(\mathbf{k}, i\omega_n) - \hat{P}^{\dagger}(\mathbf{k})\left(\Sigma(\mathbf{k}, i\omega_n) - \Sigma_{DC}\right)\hat{P}(\mathbf{k}), \tag{9}$$

into the non-interacting lattice GF G_0 given by the first term of (5), with the DC for the self-energy defined by (8).

The DMFT is based on the key observation of Ref. [143] that one may define a (non-trivial) infinite-dimensional limit of (5), and that the electronic self-energy becomes purely local in this limit, i. e., $\mathbf{k}$-independent[6], $\Sigma(\mathbf{k}, i\omega_n) \xrightarrow{d\to\infty} \Sigma(i\omega_n)$. Such single-site self-energy is given by the summation over irreducible (skeleton) Feynman diagrams involving only the single-site GF and the local vertex $\hat{U}$. The coupling between a representative correlated shell o and an effective electronic "bath" representing the rest of system is then given by the bath Green's function:

$$\mathcal{G}^{-1}_0(i\omega_n) = \left[\sum_{\mathbf{k}} \hat{P}(\mathbf{k})G(\mathbf{k}, i\omega_n)\hat{P}^{\dagger}(\mathbf{k})\right]^{-1} + \Sigma(i\omega_n) = i\omega_n - \hat{\epsilon} - \Delta(i\omega_n), \tag{10}$$

where $\hat{\epsilon}$ are bare (non-interacting) single-site level positions, $\Delta(i\omega_n)$ is the hybridization function due to hopping between the site and electronic bath. The single-site problem in the correlated

[5]The imaginary time/frequency domain is often used in DMFT calculations for the technical reasons outlined in Sec. A.2, though it is not necessary.

[6]In the case of DFT+U Hamiltonian (5) this approximation is applied to the self-energy $\Sigma(\mathbf{k}, i\omega_n)$ in the correlated subspace, while Σ^{KS} can still be $\mathbf{k}$ dependent due to the projectors $\hat{P}(\mathbf{k})$.

subspace is completely defined by (10) and on-site Coulomb replusion

$$\hat{H}_U^{(o)} = \sum_{1,2,3,4} \langle 12|U|34\rangle d_1^\dagger d_2^\dagger d_4 d_3$$

(omitting the irrelevant site index o in d and $d^\dagger$). The lattice problem is thus mapped into an auxilary *quantum impurity problem* (QIP) [144] for a single correlated shell, which is fully analogous to the standard Anderson impurity model (AIM). However, in contrast to the usual AIM, $\Delta(i\omega_n)$ is not given by the hybridization of non-interacting bands; it should be rather viewed as a dynamical mean-field implicitly depended on the single-site self-energy through eqs. (9-10). By solving the QIP, i. e., by summing (all or subset of) local Feynman diagrams one obtains the impurity GF and self-energy:

$$\left\{\mathcal{G}(i\omega_n), \hat{H}_U^{(o)}\right\} \to \{G_{imp}(i\omega_n), \Sigma_{imp}(i\omega_n)\}\,. \tag{11}$$

One then employs the standard recipe to close the mean-field cycle as shown in Fig. 13: the obtained impurity self-energy is inserted for all correlated shells, $\Sigma(\mathbf{k}, i\omega_n) \equiv \Sigma_{imp}(i\omega_n)$ allowing to update the chemical potential μ and to recalculate the mean field $\mathcal{G}_0$ by eqs. (9-10). This cycle is iterated until the self-consistency is reached: the QIP solved for the mean-field $\mathcal{G}_0$ results in the same self-energy Σ that was used to obtain this mean-field through (9-10). Alternatively, the same self-consistency condition is represented by $G_{imp}(i\omega_n) = G_{loc}(i\omega_n)$, where

$$G_{loc}(i\omega_n) = \sum_{\mathbf{k}} \hat{P}(\mathbf{k}) G(\mathbf{k}, i\omega_n) \hat{P}^\dagger(\mathbf{k}) \tag{12}$$

is the local GF of lattice problem. The problem defined by the Hamiltonian (5) is thus exactly solved in the limit of infinite lattice connectivity, as can be also shown explicitly, see [145]. As for any mean-field approach the usefulness of DMFT method is based on its ability to describe the realistic 3d lattices, for which the single-site approximation $\Sigma(\mathbf{k}, i\omega_n) \to \Sigma(i\omega_n)$ appears to be rather reasonable, though it is not quantitatively exact. At the same time the single-site dynamics due to electronic correlations is fully included in DMFT; this explains its success in reproducing such non-perturbative phenomena as the Mott transition. The method captures not only the insulating $U/W \to \infty$ and non-interacting $U/W \to 0$ limits (where W is the bandwidth of non-interacting bands $\epsilon_{\nu k}$ in (5)) but also all intermediate regimes given by finite U/W.

For 2d and quasi-2d systems the single-site DMFT is generally not an adequate approximation. The $\mathbf{k}$ dependence of the self-energy is key to describe, for example, the physics of layered cuprate superconductors, in particular, their PES [146]. This problem was addressed by cluster extensions of the single-site DMFT, which were formulated in both the real and reciprocal spaces [147, 148, 149]. The single-site QIP (11) is thus generalized to the corresponding cluster problem. Such generalization increases dramatically the computational cost of solving the QIP, hence, the cluster methods are not generally applicable to full d and f shells; they have been extensively applied to quasi-1band systems like layered cuprates. Another more recent effort in development of extended-DMFT frameworks [150, 151, 152] is based on applying the single-site approximation to two-electron correlation functions (like the vertex function) while keeping the $\mathbf{k}$-dependence of the one-electron self-energy. These approaches are promising for applications to multiband systems, though they are still currently too heavy for applications in the cases considered in this highlight, when many-electron effects for the full d shell need to be taken into account.

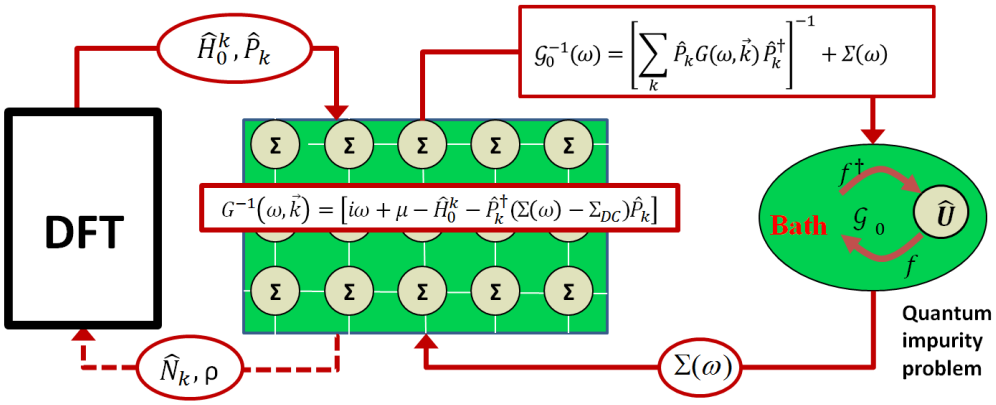

Figure 13: Schematic diagram of the DFT+DMFT method. The initial input from the DFT part is the quadratic KS Hamiltonain $\hat{H}_0$ and projectors $\hat{P}$ between the KS space and correlated subspace. The right-hand side represents the DMFT cycle with the lattice problem mapped into the quantum-impurity one using eq. 10; the calculated impurity self-energy subsequently is inserted back to the lattice, eq. 9. The updated DMFT density matrix can be inserted back to the DFT part (dashed arrow) to take into account modifications of the charge density and, therefore, $\hat{H}_0$, due to correlations; this results in a DFT+DMFT framework that is self-consistent in the charge density.

A.2 The quantum impurity problem

The QIP problem schematically given by eq. 11 is a true many-electron problem, though a single-site one, and represents, in fact, a numerical "bottleneck" of the DFT+DMFT framework. In the imaginary-time path integral formalism (see e.g. [153]) it reads

$$G_{\alpha\alpha'}(\tau_0 - \tau_1) = \frac{1}{Z} \int \mathcal{D}[d, d^\dagger] d_\alpha(\tau_0) d^\dagger_{\alpha'}(\tau_1) \exp[-S], \tag{13}$$

where $\mathcal{D}[d, d^\dagger]$ is the path integration over all impurity degrees of freedom and

$$Z = \int \mathcal{D}[d, d^\dagger] \exp[-S] \tag{14}$$

is the impurity partition function, S is the impurity action:

$$S = \sum_{\alpha_1\alpha_2} \int d\tau \int d\tau' f^\dagger_{\alpha_1}(\tau) \left[\mathcal{G}_0^{-1}(\tau - \tau')\right]_{\alpha_1\alpha_2} f_{\alpha_2}(\tau') + \int d\tau \hat{H}_U^{(o)}(\tau). \tag{15}$$

Many-body methods to evaluate (13) represent a large research field initiated by early studies of AIM and very actively developed at present, in particular, to provide efficient quantum-impurity "solvers" for the DMFT framework. They will not be reviewed here in any details; we will only briefly outline main strategies for solving the QIP and provide some useful references.

The methods dealing with QIP can be divided into numerically-exact and approximate analytical kinds. Among the former one may especially mention stochastic quantum Monte Carlo (QMC) methods; a breakthrough in this domain has been achieved by so-called "continuous-time" (CT) QMC methods [154] (see review [52] on its applications to the fermionic QIP). The most popular CT-QMC approaches are based on an expansion of the partition function (14) in powers of

$\hat{H}_U^{(o)}$ [155] or, alternatively, in powers of the hybridization function $\Delta(\tau)$ [156], see eq. 10. One subsequently sums up various diagrammatic contributions into GF (13) and other correlation function in accordance with their relative weight in Z by employing a Monte Carlo importance sampling. In contrast to the older QMC approach of Hirch and Fye [157] based on discretization of the integrals over τ in (15) the CT-QMC approach is free from the discretization error and can treat more complex interaction vertices $\hat{H}_U^{(o)}$. All these QMC methods generally work in the imaginary-time/imaginary-frequency domain, hence, the resulting GF needs to be analytically continued to the real-energy axis to obtain an experimentally-observable real-frequency spectra.

The hybridization-expansion CT-QMC technique employed as a quantum-impurity solver in the DFT+DMFT calculations presented in this review. This approach is sufficiently computationally efficient to solve the QIP for the whole Fe $3d$ shell. Particularly, the case of simplified, "density-density" Coulomb vertex $\hat{H}_U^{(o)}$ reducible to the form $\sum_{\alpha\alpha'} U_{\alpha\alpha'}\hat{n}_\alpha\hat{n}_{\alpha'}$ allows to employ the fast "segment-picture" algorithm [156, 52], reducing the computational effort very significantly. The density-density approximation neglects some potentially important matrix elements of the Coulomb vertex[7] and thus introduces a system-dependent error. In the case of moderately-correlated metal like iron it does not affect the qualitative picture, but is still quantitatively important (see Appendix B); for strongly-correlated systems as, for example, FeSe [158] this approximation may lead to qualitatively wrong results. Calculation with the full 4-index vertex are much more computationally demanding, but still nowdays possible thanks to a recent development of fast algorithms [159, 160].

Another popular numerically-exact approach, the exact diagonalization technique [161], see also [162, 163] for more recent developments. It is based on representing the hybridization function by a set of auxiliary discrete levels $\{\epsilon_b\}$ of the bath mixing with the impurity states, $\Delta_{\alpha\alpha'}(\omega) \sim \sum_b \frac{V_{b\alpha}V^\dagger_{b\alpha'}}{\omega-\epsilon_b}$. The resulting large Hamiltonian including both impurity and bath states is subsequently diagonalized by Lanczos or similar techniques allowing to compute the impurity GF from obtained eigenvalues and eigenstates. Among the exact methods one should also mention the numerical renormalization-group and density-matrix renormalization-group methods [164, 165].

Analytical approaches are generally applicable only in certain regimes (strong or weak coupling). Weak-coupling methods are suitable for metallic phases; they are based on the standard Wick theorem and subsequent summation of a certain subset of Feynmann diagrams, like, for example, the fluctuation-exchange approximation [44, 166, 167], which has been extensively applied to spectral properties of iron and nickel [168, 47, 48, 169]. Among numerous other analytical methods one may also mention the "slave" particle approach [170, 171, 172, 118] providing an economical and numerically efficient treatment of the quasiparticle renormalization in multiband systems. The obvious advantage of these analytical techniques is their computational efficiency. They can also easily evaluate the GF and, hence, the measurable one-electron spectra, at the real-frequency axis.

Finally, the simplest approach to solving the QIP consists in employing the static Hartree-Fock approximation; in this case DFT+DMFT is reduced to the popular LDA+U method [15, 121].

[7] For example, the "spin-flip" contributions to $\hat{H}_U^{(o)}$ of the form $d^\dagger_{m\uparrow}d^\dagger_{m'\downarrow}d_{m'\uparrow}d_{m\downarrow}$ cannot be reduced to a density-density form.

A.3 Charge density and total energy

As a result of the DMFT cycle (Fig. 13) one obtains the converged interacting lattice GF (9) in the KS space. The corresponding density matrix

$$N^{\mathbf{k}}_{\nu\nu'} = \sum_n G_{\nu\nu'}(\mathbf{k}, i\omega_n) e^{i\omega_n 0^+} \tag{16}$$

gives the contribution of KS bands in $\mathcal{W}$ to the charge density. Therefore, the charge density $n(\mathbf{r})$ is affected by many-electron effects through the DMFT self-energy $\Sigma(i\omega_n)$ entering into $G(\mathbf{k}, i\omega_n)$; the KS one-electron potential being a functional of $n(\mathbf{r})$ is thus modified as well. Hence, the one-electron part H_0 of the DFT+U Hamiltonain (5) comes out to be implicitly dependent on $\Sigma(i\omega_n)$.

This observation led to formulation of the charge self-consistent DFT+DMFT framework, in which $n(\mathbf{r})$ and H_0 are consistently updated to take into account the impact of correlations as shown in the left-hand side of Fig. 13. In practice, $\hat{N}^{\mathbf{k}}$ in the KS basis is submitted back to the DFT part; the corresponding contribution to $n(\mathbf{r})$ is then calculated through the expansion of $\psi_{\mathbf{k}\nu}$ in the basis of a given band-structure method. Several such self-consistent DFT+DMFT frameworks have been implemented recently [132, 46, 173, 174, 175, 176, 177].

In this self-consistent framework the DMFT self-consistency condition, $G_{loc} \equiv G_{imp}$, as well as the relation between the KS potential and electronic density are derived by extremization of the following DFT+DMFT grand potential [106] :

$$\begin{aligned} \Omega\left[n(\mathbf{r}), G_{loc}, \Delta\Sigma, \hat{\epsilon}\right] = &- \operatorname{Tr}\ln\left[i\omega_n + \mu - H_0 - \Delta\Sigma\right] - \operatorname{Tr}\left[G_{loc}\Delta\Sigma\right] \\ &+ \sum_{\mathbf{R}} \left[\Phi_{imp}[G_{loc}(\mathbf{R})] - \Phi_{DC}[G_{loc}(\mathbf{R})]\right] + \Omega_r[n(\mathbf{r})] \\ &\equiv \Delta\Omega\left[G_{loc}, \Delta\Sigma, V_{KS}\right] + \Omega_r[n(\mathbf{r})], \end{aligned} \tag{17}$$

where $\Delta\Sigma$ is the difference between the impurity self-energy Σ_{imp} and the double counting correction (8), $\Phi_{imp}[G_{loc}(\mathbf{R})]$ is the DMFT interaction energy functional for the site $\mathbf{R}$, $\Phi_{DC}[G^{loc}_{\mathbf{R}}]$ is the corresponding functional for the double-counting correction. The last term $\Omega_r[n(\mathbf{r})]$ depends only on the electronic charge density $n(\mathbf{r})$ and comprises the electron-nuclei, Hartree and exchange-correlation contribution, while all other terms collected in $\Delta\Omega\left[G_{loc}, \Delta\Sigma, V_{KS}\right]$ do not have an explicit dependence on $n(\mathbf{r})$. From the zero-temperature limit of (17) one derives [178] the following expression for the total energy:

$$E_{DFT+DMFT} = \sum_{\mathbf{k}\nu} \epsilon_{\mathbf{k}\nu} N^{\mathbf{k}}_{\nu\nu} + \langle H_U \rangle - E_{DC} + E_{en}[n(\mathbf{r})] + E_H[n(\mathbf{r})] + E_{xc}[n(\mathbf{r})], \tag{18}$$

where E_{en}, E_H, E_{xc} are the standard DFT electron-nuclei, Hartree and exchange-correlation contributions evaluated from the charge density $n(\mathbf{r})$ that includes the DMFT correction. The interaction energy $\langle H_U \rangle$ can be evaluated from the self-energy using the Migdal formula $\langle H_U \rangle = \frac{1}{2}\operatorname{Tr}\left[\Sigma_{imp} G_{imp}\right]$, alternatively, the expectation value $\langle d^\dagger_1 d^\dagger_2 d_3 d_4 \rangle$ can be directly measured, e. g., by using QMC quantum-impurity solvers.

Instead of the self-consistent charge density $n(\mathbf{r})$ one may employ in (18) the DFT one, $n_{DFT}(\mathbf{r})$ resulting in the so-called "one-shot DMFT" scheme. The impact of the self-consistency in

charge density on the DFT+DMFT total-energy and spectra has been studied in a number of works [173, 175, 179, 180, 181], though a consistent assessment for the full range of correlation strength is still lacking. However, the charge-density self-consistency seems to important for localized systems as γ-Ce and Ce oxides [173] and VO_2 [180]. The possible reason pointed out by Ref. [181] is that the occupancy of $\psi_{\mathbf{k}\nu}$ states is very different in the localized limit as compared to a metallic band structure predicted by DFT. In the former case the KS states $\mathbf{k}\nu$ of correlated bands will be all roughly half-filed due to the contribution of corresponding lower Hubbard band. In DFT the KS states $\mathbf{k}\nu$ are occupied below E_F and empty above, hence, the occupancy varies strongly in the $\mathbf{k}$ space. Another important effect of the charge-density self-consistency is an overall lower sensitivity of the result to the choice of DC; changes in DC seem to be compensated by the corresponding modifications in V_{KS} [175].

B The impact of density-density approximation: a benchmark

In this appendix we illustrate the impact of density-density approximation for the local Coulomb interaction by performing DFT+DMFT calculations with and without this approximation for the bcc α and hcp ϵ iron phases at the Earth's core condition. Self-consistent in the charge density DFT+DMFT calculations (Sec. A.3) were thus carried out for the perfect bcc and hcp lattices at the atomic volume of 7.05 Å^3/atom expected for the inner core of Earth and the temperature of 5800 K. The on-site Coulomb interaction was defined by the parameters U =5.0 eV, J_H =0.93 eV previously used in the study of ϵ-Fe by Ref. [90]; the same choice for the energy window ([-10.8 eV, 4.0 eV] around the Fermi level) was also employed for the Kohn-Sham states used to construct Wannier orbitals representing Fe 3d states. The DMFT impurity problem was solved by the hybridization-expansion quantum Monte Carlo impurity solver using its segment-picture version [156, 52] in the case of density-density (Ising) vertex and the implementation of Seth *et al.* [182] in the case of full rotationally-invariant one.

The resulting DMFT self-energies for both phases are compared in Fig. 14. For both bcc and hcp-Fe the use of density-density approximation results in a systematic underestimation of the magnitude of scattering $|Im\Sigma(i\omega_n)|$, which is, however, more pronounced in the case of more correlated bcc. Qualitative features, like the e_g orbitals markedly more correlated than the t_{2g} ones in bcc-Fe as well as a uniform Fermi-liquid behavior of all orbitals in hcp, are well captured within the density-density approximation. We have also calculated the transport using the approach outlined in Sec. 3.2 and these self-energies analytically continued to the real-energy axis. The electrical and thermal conductivities for bcc are found to be overestimated by 40% and 29%, respectively, due to the density-density approximation. As expected, the impact of this approximation for the less-correlated hcp phase is smaller and amounts to 33% and 23%, respectively. Hence, though the use of full vertex does not lead to qualitative changes it is still found to be important for quantitative results.

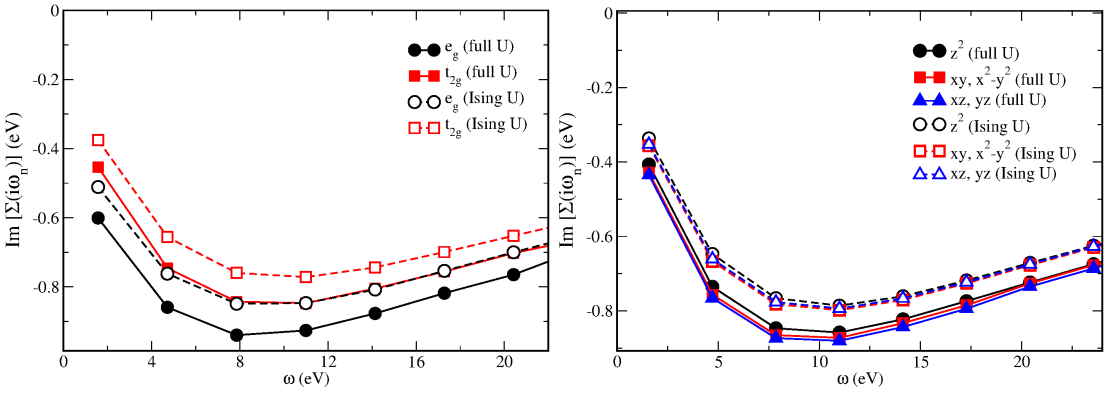

Figure 14: Left panel: The imaginary part of DMFT self-energy on the Matusbara grid for the non-degenerate orbitals of the Fe 3d shell in the bcc structure calculated with the rotationally-invariant (filled symbols) and density-density (empty symbols) local Coulomb interaction, respectively. Right panel: the same for the hcp structure.

References

[1] H. K. D. H. Bhadeshia and R. Honeycombe, *Steels: Microstructure and Properties*, Butterworth-Heinemann, New York, 2006.

[2] J. Neuhaus *et al.*, Role of vibrational entropy in the stabilization of the high-temperature phases of iron, Phys. Rev. B **89**, 184302 (2014).

[3] C. Zener, Impact of Magnetism Upon Metallurgy, Trans. A.I.M.M.E **203**, 619 (1955).

[4] Y. Tsunoda, Spin-density wave in cubic γ-Fe and γ-$Fe_{100-x}Co_x$ precipitates in Cu, Journal of Physics: Condensed Matter **1**, 10427 (1989).

[5] D. Bancroft, E. L. Peterson, and S. Minshall, Polymorphism of Iron at High Pressure, Journal of Applied Physics **27**, 291 (1956).

[6] J. C. Jamieson and A. W. Lawson, X-Ray Diffraction Studies in the 100 Kilobar Pressure Range, Journal of Applied Physics **33**, 776 (1962).

[7] H. K. Mao, Y. Wu, L. C. Chen, J. F. Shu, and A. P. Jephcoat, Static compression of iron to 300 GPa and $Fe_{0.8}Ni_{0.2}$ alloy to 260 GPa: Implications for composition of the core, Journal of Geophysical Research: Solid Earth **95**, 21737 (1990).

[8] L. Stixrude, Structure of Iron to 1 Gbar and 40 000 K, Phys. Rev. Lett. **108**, 055505 (2012).

[9] K. Shimizu *et al.*, Superconductivity in the non-magnetic state of iron under pressure, Nature **412**, 316 (2000).

[10] I. I. Mazin, D. A. Papaconstantopoulos, and M. J. Mehl, Superconductivity in compressed iron: Role of spin fluctuations, Phys. Rev. B **65**, 100511 (2002).

[11] G. Cort, R. D. Taylor, and J. O. Willis, Search for magnetism in hcp epsilon-Fe, Journal of Applied Physics **53**, 2064 (1982).

[12] A. B. Papandrew *et al.*, Absence of Magnetism in Hcp Iron-Nickel at 11 K, Phys. Rev. Lett. **97**, 087202 (2006).

[13] A. T. Holmes, D. Jaccard, G. Behr, Y. Inada, and Y. Onuki, Unconventional superconductivity and non-Fermi liquid behaviour of ϵ-iron at high pressure, Journal of Physics: Condensed Matter **16**, S1121 (2004).

[14] C. S. Yadav *et al.*, Effect of pressure cycling on iron: Signatures of an electronic instability and unconventional superconductivity, Phys. Rev. B **88**, 054110 (2013).

[15] V. I. Anisimov, J. Zaanen, and O. K. Andersen, Band theory and Mott insulators: Hubbard U instead of Stoner I, Phys. Rev. B **44**, 943 (1991).

[16] M. Cococcioni and S. de Gironcoli, Linear response approach to the calculation of the effective interaction parameters in the LDA + U method, Phys. Rev. B **71**, 035105 (2005).

[17] A. Belozerov and V. Anisimov, Coulomb interaction parameters in bcc iron: an LDA+ DMFT study, Journal of Physics: Condensed Matter **26**, 375601 (2014).

[18] T. Miyake and F. Aryasetiawan, Screened Coulomb interaction in the maximally localized Wannier basis, Phys. Rev. B **77**, 085122 (2008).

[19] T. Miyake, F. Aryasetiawan, and M. Imada, *Ab initio* procedure for constructing effective models of correlated materials with entangled band structure, Phys. Rev. B **80**, 155134 (2009).

[20] J. E. Han, M. Jarrell, and D. L. Cox, Multiorbital Hubbard model in infinite dimensions: Quantum Monte Carlo calculation, Phys. Rev. B **58**, R4199 (1998).

[21] L. de' Medici, J. Mravlje, and A. Georges, Janus-Faced Influence of Hund's Rule Coupling in Strongly Correlated Materials, Phys. Rev. Lett. **107**, 256401 (2011).

[22] K. Haule and G. Kotliar, Coherence-incoherence crossover in the normal state of iron oxypnictides and importance of Hund's rule coupling, New Journal of Physics **11**, 025021 (2009).

[23] A. Georges, L. de' Medici, and J. Mravlje, Strong Correlations from Hund's Coupling, Annual Review of Condensed Matter Physics **4**, 137 (2013).

[24] R. Frésard and G. Kotliar, Interplay of Mott transition and ferromagnetism in the orbitally degenerate Hubbard model, Phys. Rev. B **56**, 12909 (1997).

[25] R. Maglic, Van Hove Singularity in the Iron Density of States, Phys. Rev. Lett. **31**, 546 (1973).

[26] V. Y. Irkhin, M. I. Katsnelson, and A. V. Trefilov, On the microscopic model of Fe and Ni: the possible breakdown of the ferromagnetic fermi-liquid picture, Journal of Physics: Condensed Matter **5**, 8763 (1993).

[27] C. S. Wang, B. M. Klein, and H. Krakauer, Theory of Magnetic and Structural Ordering in Iron, Phys. Rev. Lett. **54**, 1852 (1985).

[28] D. J. Singh, W. E. Pickett, and H. Krakauer, Gradient-corrected density functionals: Full-potential calculations for iron, Phys. Rev. B **43**, 11628 (1991).

[29] C. Amador, W. R. L. Lambrecht, and B. Segall, Application of generalized gradient-corrected density functionals to iron, Phys. Rev. B **46**, 1870 (1992).

[30] H. C. Hsueh *et al.*, Magnetism and mechanical stability of α-iron, Phys. Rev. B **66**, 052420 (2002).

[31] I. Leonov, A. I. Poteryaev, V. I. Anisimov, and D. Vollhardt, Calculated phonon spectra of paramagnetic iron at the α-γ phase transition, Phys. Rev. B **85**, 020401 (2012).

[32] B. L. Gyorffy, A. J. Pindor, J. Staunton, G. M. Stocks, and H. Winter, A first-principles theory of ferromagnetic phase transitions in metals, Journal of Physics F: Metal Physics **15**, 1337 (1985).

[33] S. V. Okatov, A. R. Kuznetsov, Y. N. Gornostyrev, V. N. Urtsev, and M. I. Katsnelson, Effect of magnetic state on the $\gamma-\alpha$ transition in iron: First-principles calculations of the Bain transformation path, Phys. Rev. B **79**, 094111 (2009).

[34] H. Zhang, B. Johansson, and L. Vitos, Density-functional study of paramagnetic iron, Phys. Rev. B **84**, 140411 (2011).

[35] F. Körmann *et al.*, Free energy of bcc iron: Integrated ab initio derivation of vibrational, electronic, and magnetic contributions, Phys. Rev. B **78**, 033102 (2008).

[36] A. V. Ruban and V. I. Razumovskiy, Spin-wave method for the total energy of paramagnetic state, Phys. Rev. B **85**, 174407 (2012).

[37] I. Abrikosov, A. Ponomareva, P. Steneteg, S. Barannikova, and B. Alling, Recent progress in simulations of the paramagnetic state of magnetic materials, Current Opinion in Solid State and Materials Science **20**, 85 (2016).

[38] Y. Liu *et al.*, Direct method for calculating temperature-dependent transport properties, Phys. Rev. B **91**, 220405 (2015).

[39] V. Drchal, J. Kudrnovský, D. Wagenknecht, I. Turek, and S. Khmelevskyi, Transport properties of iron at Earth's core conditions: The effect of spin disorder, Phys. Rev. B **96**, 024432 (2017).

[40] J. Schäfer, M. Hoinkis, E. Rotenberg, P. Blaha, and R. Claessen, Fermi surface and electron correlation effects of ferromagnetic iron, Phys. Rev. B **72**, 155115 (2005).

[41] I. Leonov, A. I. Poteryaev, V. I. Anisimov, and D. Vollhardt, Electronic Correlations at the α-γ Structural Phase Transition in Paramagnetic Iron, Phys. Rev. Lett. **106**, 106405 (2011).

[42] I. Leonov *et al.*, Electronic correlations determine the phase stability of iron up to the melting temperature, Scientific Reports **4**, 5585 (2014).

[43] Q. Han, T. Birol, and K. Haule, Phonon Softening due to Melting of the Ferromagnetic Order in Elemental Iron, Phys. Rev. Lett. **120**, 187203 (2018).

[44] M. I. Katsnelson and A. I. Lichtenstein, LDA++ approach to the electronic structure of magnets: correlation effects in iron, Journal of Physics: Condensed Matter **11**, 1037 (1999).

[45] A. I. Lichtenstein, M. I. Katsnelson, and G. Kotliar, Finite-Temperature Magnetism of Transition Metals: An *ab initio* Dynamical Mean-Field Theory, Phys. Rev. Lett. **87**, 067205 (2001).

[46] J. Minár *et al.*, Multiple-scattering formalism for correlated systems: A KKR-DMFT approach, Phys. Rev. B **72**, 045125 (2005).

[47] A. Grechnev *et al.*, Theory of bulk and surface quasiparticle spectra for Fe, Co, and Ni, Phys. Rev. B **76**, 035107 (2007).

[48] J. Sánchez-Barriga *et al.*, Strength of Correlation Effects in the Electronic Structure of Iron, Phys. Rev. Lett. **103**, 267203 (2009).

[49] A. Hausoel *et al.*, Local magnetic moments in iron and nickel at ambient and Earth's core conditions, Nature Communications **8**, 16062 (2017).

[50] A. A. Katanin *et al.*, Orbital-selective formation of local moments in α-iron: First-principles route to an effective model, Phys. Rev. B , 045117 (2010).

[51] P. A. Igoshev, A. V. Efremov, A. I. Poteryaev, A. A. Katanin, and V. I. Anisimov, Magnetic fluctuations and effective magnetic moments in γ-iron due to electronic structure peculiarities, Phys. Rev. B **88**, 155120 (2013).

[52] E. Gull *et al.*, Continuous-time Monte Carlo methods for quantum impurity models, Rev. Mod. Phys. **83**, 349 (2011).

[53] L. Sponza *et al.*, Self-energies in itinerant magnets: A focus on Fe and Ni, Phys. Rev. B **95**, 041112 (2017).

[54] S. Biermann, F. Aryasetiawan, and A. Georges, First-Principles Approach to the Electronic Structure of Strongly Correlated Systems: Combining the *GW* Approximation and Dynamical Mean-Field Theory, Phys. Rev. Lett. **90**, 086402 (2003).

[55] J. M. Tomczak, P. Liu, A. Toschi, G. Kresse, and K. Held, Merging GW with DMFT and non-local correlations beyond, The European Physical Journal Special Topics **226**, 2565 (2017).

[56] G. Steinle-Neumann, L. Stixrude, and R. E. Cohen, Magnetism in dense hexagonal iron, Proceedings of the National Academy of Sciences **101**, 33 (2004).

[57] A. Monza *et al.*, Iron Under Pressure: "Kohn Tweezers" and Remnant Magnetism, Phys. Rev. Lett. **106**, 247201 (2011).

[58] G. Steinle-Neumann, L. Stixrude, and R. E. Cohen, First-principles elastic constants for the hcp transition metals Fe, Co, and Re at high pressure, Phys. Rev. B **60**, 791 (1999).

[59] X. Sha and R. E. Cohen, First-principles studies of electrical resistivity of iron under pressure, Journal of Physics: Condensed Matter **23**, 075401 (2011).

[60] A. Dewaele *et al.*, Quasihydrostatic Equation of State of Iron above 2 Mbar, Phys. Rev. Lett. **97**, 215504 (2006).

[61] L. V. Pourovskii, J. Mravlje, M. Ferrero, O. Parcollet, and I. A. Abrikosov, Impact of electronic correlations on the equation of state and transport in ε-Fe, Phys. Rev. B **90**, 155120 (2014).

[62] M. Casula *et al.*, Low-Energy Models for Correlated Materials: Bandwidth Renormalization from Coulombic Screening, Phys. Rev. Lett. **109**, 126408 (2012).

[63] L. V. Pourovskii *et al.*, Electronic properties and magnetism of iron at the Earth's inner core conditions, Phys. Rev. B **87**, 115130 (2013).

[64] K. Glazyrin *et al.*, Importance of Correlation Effects in hcp Iron Revealed by a Pressure-Induced Electronic Topological Transition, Phys. Rev. Lett. **110**, 117206 (2013).

[65] V. G. Vaks and A. V. Trefilov, Anomalies of phonon spectra and anharmonic effects in metals and alloys due to proximity of the Fermi level to singular points of band structure, Journal of Physics: Condensed Matter **3**, 1389 (1991).

[66] D. L. Novikov *et al.*, Anisotropy of thermal expansion and electronic topological transitions in Zn and Cd under pressure, Phys. Rev. B **59**, 4557 (1999).

[67] M. I. Katsnelson and A. V. Trefilov, Fermi-liquid theory of electronic topological transitions and screening anomalies in metals, Phys. Rev. B **61**, 1643 (2000).

[68] Q. Feng, M. Ekholm, F. Tasnádi, H. J. M. Jönsson, and I. A. Abrikosov, Topological transitions of the Fermi surface of osmium under pressure: an LDA+DMFT study, New Journal of Physics **19**, 033020 (2017).

[69] A. Dewaele and G. Garbarino, Low temperature equation of state of iron, Applied Physics Letters **111**, 021903 (2017).

[70] F. Birch, Elasticity and constitution of the Earth's interior, Journal of Geophysical Research **57**, 227 (1952).

[71] A. M. Dziewonski and D. L. Anderson, Preliminary reference Earth model, Physics of the Earth and Planetary Interiors **25**, 297 (1981).

[72] W. Lowrie, *Fundamentals of Geophysics*, Cambridge University Press, 2 edition, 2007.

[73] R. Boehler, Temperatures in the Earth's core from melting-point measurements of iron at high static pressures, Nature **363**, 534 (1993).

[74] D. Alfé, M. J. Gillan, and G. D. Price, The melting curve of iron at the pressures of the Earth's core from ab initio calculations, Nature **401**, 462 (1999).

[75] A. B. Belonoshko, R. Ahuja, and B. Johansson, Quasi˘Ab Initio Molecular Dynamic Study of Fe Melting, Phys. Rev. Lett. **84**, 3638 (2000).

[76] H. Tkalčić, Complex inner core of the Earth: The last frontier of global seismology, Reviews of Geophysics **53**, 59 (2015).

[77] B. Buffett, Geomagnetism under scrutiny, Nature **485**, 319 (2012).

[78] M. Pozzo, C. Davies, D. Gubbins, and D. Alfè, Thermal and electrical conductivity of iron at Earth's core conditions, Nature **485**, 355 (2012).

[79] S. Tateno, K. Hirose, Y. Ohishi, and Y. Tatsumi, The Structure of Iron in Earth's Inner Core, Science **330**, 359 (2010).

[80] S. Tateno, K. Hirose, T. Komabayashi, H. Ozawa, and Y. Ohishi, The structure of Fe-Ni alloy in Earth's inner core, Geophysical Research Letters **39**, L12305 (2012).

[81] S. Anzellini, A. Dewaele, M. Mezouar, P. Loubeyre, and G. Morard, Melting of Iron at Earth's Inner Core Boundary Based on Fast X-ray Diffraction, Science **340**, 464 (2013).

[82] L. Dubrovinsky *et al.*, Body-Centered Cubic Iron-Nickel Alloy in Earth's Core, Science **316**, 1880 (2007).

[83] R. Hrubiak, Y. Meng, and G. Shen, Experimental evidence of a body centered cubic iron at the Earth's core condition, arXiv:1804.05109, 2018.

[84] L. Dubrovinsky, N. Dubrovinskaia, and V. B. Prakapenka, Is iron at the Earth's core conditions hcp-structured?, Física de la Tierra **23**, 73 (2011).

[85] A. S. Mikhaylushkin *et al.*, Pure Iron Compressed and Heated to Extreme Conditions, Phys. Rev. Lett. **99**, 165505 (2007).

[86] L. Vočaldo *et al.*, Possible thermal and chemical stabilization of body-centred-cubic iron in the Earth's core, Nature **424**, 536 (2003).

[87] B. K. Godwal, F. González-Cataldo, A. Verma, L. Stixrude, and R. Jeanloz, Stability of iron crystal structures at 0.3-1.5 TPa, Earth and Planetary Science Letters **409**, 299 (2015).

[88] A. B. Belonoshko *et al.*, Stabilization of body-centred cubic iron under inner-core conditions, Nature Geoscience **10**, 312 (2017).

[89] O. Y. Vekilova, L. V. Pourovskii, I. A. Abrikosov, and S. I. Simak, Electronic correlations in Fe at Earth's inner core conditions: Effects of alloying with Ni, Phys. Rev. B **91**, 245116 (2015).

[90] L. V. Pourovskii, J. Mravlje, A. Georges, S. I. Simak, and I. A. Abrikosov, Electron-electron scattering and thermal conductivity of ϵ-iron at Earth's core conditions, New Journal of Physics **19**, 073022 (2017).

[91] J. Mravlje *et al.*, Coherence-Incoherence Crossover and the Mass-Renormalization Puzzles in Sr_2RuO_4, Phys. Rev. Lett. **106**, 096401 (2011).

[92] P. Zhang, R. Cohen, and K. Haule, Effects of electron correlations on transport properties of iron at Earth's core conditions, Nature **517**, 605 (2015).

[93] P. Zhang, R. Cohen, and K. Haule, Retraction: Effects of electron correlations on transport properties of iron at Earth's core conditions, Nature **536**, 112 (2016).

[94] A. V. Chubukov and D. L. Maslov, First-Matsubara-frequency rule in a Fermi liquid. I. Fermionic self-energy, Phys. Rev. B **86**, 155136 (2012).

[95] C. Berthod *et al.*, Non-Drude universal scaling laws for the optical response of local Fermi liquids, Phys. Rev. B **87**, 115109 (2013).

[96] A. V. Ruban, A. B. Belonoshko, and N. V. Skorodumova, Impact of magnetism on Fe under Earth's core conditions, Phys. Rev. B **87**, 014405 (2013).

[97] W. F. McDonough and S.-s. Sun, The composition of the Earth, Chemical Geology **120**, 223 (1995).

[98] T. Lay, J. Hernlund, and B. Buffett, Core-mantle boundary heat flow, Nature Geoscience **1**, 25 (2008).

[99] P. Olson, The New Core Paradox, Science **342**, 431 (2013).

[100] F. Stacey and D. Loper, A revised estimate of the conductivity of iron alloy at high pressure and implications for the core energy balance, Physics of the Earth and Planetary Interiors **161**, 13 (2007).

[101] N. de Koker, G. Steinle-Neumann, and V. Vlček, Electrical resistivity and thermal conductivity of liquid Fe alloys at high P and T, and heat flux in Earth's core, Proc. Natl. Acad. Sci. U. S. A. **109**, 4070 (2012).

[102] B. Romanowicz, X.-D. Li, and J. Durek, Anisotropy in the Inner Core: Could It Be Due To Low-Order Convection?, Science **274**, 963 (1996).

[103] B. A. Buffett, Onset and orientation of convection in the inner core, Geophysical Journal International **179**, 711 (2009).

[104] M. Monnereau, M. Calvet, L. Margerin, and A. Souriau, Lopsided Growth of Earth's Inner Core, Science **328**, 1014 (2010).

[105] M. Pozzo, C. Davies, D. Gubbins, and D. Alfè, Thermal and electrical conductivity of solid iron and ironsilicon mixtures at Earth's core conditions, Earth and Planetary Science Letters **393**, 159 (2014).

[106] G. Kotliar *et al.*, Electronic structure calculations with dynamical mean-field theory, Rev. Mod. Phys. **78**, 865 (2006).

[107] M. Aichhorn *et al.*, TRIQS/DFTTools: A TRIQS application for ab initio calculations of correlated materials, Computer Physics Communications **204**, 200 (2016).

[108] C. Ambrosch-Draxl and J. O. Sofo, Linear optical properties of solids within the full-potential linearized augmented planewave method, Computer Physics Communications **175**, 1 (2006).

[109] G. K. Madsen and D. J. Singh, BoltzTraP. A code for calculating band-structure dependent quantities, Computer Physics Communications **175**, 67 (2006).

[110] C. Herring, Simple Property of Electron-Electron Collisions in Transition Metals, Phys. Rev. Lett. **19**, 167 (1967).

[111] N. W. Ashcroft and N. D. Mermin, *Solid state physics*, chapter 13, Brooks Cole, 1976.

[112] J. Xu *et al.*, Thermal Conductivity and Electrical Resistivity of Solid Iron at Earth's Core Conditions from First Principles, Phys. Rev. Lett. **121**, 096601 (2018).

[113] J. G. O'Rourke and D. J. Stevenson, Powering Earth's dynamo with magnesium precipitation from the core, Nature **529**, 387 (2016).

[114] K. Hirose *et al.*, Crystallization of silicon dioxide and compositional evolution of the Earth's core, Nature **543**, 99 (2017).

[115] K. Haule and T. Birol, Free Energy from Stationary Implementation of the DFT + DMFT Functional, Phys. Rev. Lett. **115**, 256402 (2015).

[116] J. Bieder and B. Amadon, Thermodynamics of the α-γ transition in cerium from first principles, Phys. Rev. B **89**, 195132 (2014).

[117] J.-F. Lin, D. L. Heinz, A. J. Campbell, J. M. Devine, and G. Shen, Iron-Silicon Alloy in Earth's Core?, Science **295**, 313 (2002).

[118] G. Rohringer *et al.*, Diagrammatic routes to nonlocal correlations beyond dynamical mean field theory, Rev. Mod. Phys. **90**, 025003 (2018).

[119] I. Leonov, V. I. Anisimov, and D. Vollhardt, First-Principles Calculation of Atomic Forces and Structural Distortions in Strongly Correlated Materials, Phys. Rev. Lett. **112**, 146401 (2014).

[120] K. Haule and G. L. Pascut, Forces for structural optimizations in correlated materials within a DFT+embedded DMFT functional approach, Phys. Rev. B **94**, 195146 (2016).

[121] V. I. Anisimov, F. Aryasetiawan, and A. I. Lichtenstein, First-principles calculations of the electronic structure and spectra of strongly correlated systems: the LDA + U method, Journal of Physics: Condensed Matter **9**, 767 (1997).

[122] T. Ayral, S. Biermann, and P. Werner, Screening and nonlocal correlations in the extended Hubbard model from self-consistent combined *GW* and dynamical mean field theory, Phys. Rev. B **87**, 125149 (2013).

[123] P. Hansmann, T. Ayral, L. Vaugier, P. Werner, and S. Biermann, Long-Range Coulomb Interactions in Surface Systems: A First-Principles Description within Self-Consistently Combined *GW* and Dynamical Mean-Field Theory, Phys. Rev. Lett. **110**, 166401 (2013).

[124] N. Marzari and D. Vanderbilt, Maximally localized generalized Wannier functions for composite energy bands, Phys. Rev. B **56**, 12847 (1997).

[125] N. Marzari, A. A. Mostofi, J. R. Yates, I. Souza, and D. Vanderbilt, Maximally localized Wannier functions: Theory and applications, Rev. Mod. Phys. **84**, 1419 (2012).

[126] V. I. Anisimov *et al.*, Full orbital calculation scheme for materials with strongly correlated electrons, Phys. Rev. B **71**, 125119 (2005).

[127] F. Lechermann *et al.*, Dynamical mean-field theory using Wannier functions: A flexible route to electronic structure calculations of strongly correlated materials, Phys. Rev. B **74**, 125120 (2006).

[128] B. Amadon *et al.*, Plane-wave based electronic structure calculations for correlated materials using dynamical mean-field theory and projected local orbitals, Phys. Rev. B **77**, 205112 (2008).

[129] M. Aichhorn *et al.*, Dynamical mean-field theory within an augmented plane-wave framework: Assessing electronic correlations in the iron pnictide LaFeAsO, Phys. Rev. B **80**, 085101 (2009).

[130] O. K. Andersen and T. Saha-Dasgupta, Muffin-tin orbitals of arbitrary order, Phys. Rev. B **62**, R16219 (2000).

[131] E. Pavarini *et al.*, Mott Transition and Suppression of Orbital Fluctuations in Orthorhombic $3d^1$ Perovskites, Phys. Rev. Lett. **92**, 176403 (2004).

[132] S. Y. Savrasov and G. Kotliar, Spectral density functionals for electronic structure calculations, Phys. Rev. B **69**, 245101 (2004).

[133] R. Sakuma and F. Aryasetiawan, First-principles calculations of dynamical screened interactions for the transition metal oxides MO (M=Mn, Fe, Co, Ni), Phys. Rev. B **87**, 165118 (2013).

[134] F. Reinert and S. Hüfner, Photoemission spectroscopy-from early days to recent applications, New Journal of Physics **7**, 97 (2005).

[135] M. Casula, A. Rubtsov, and S. Biermann, Dynamical screening effects in correlated materials: Plasmon satellites and spectral weight transfers from a Green's function ansatz to extended dynamical mean field theory, Phys. Rev. B **85**, 035115 (2012).

[136] F. Aryasetiawan *et al.*, Frequency-dependent local interactions and low-energy effective models from electronic structure calculations, Phys. Rev. B **70**, 195104 (2004).

[137] P. Seth, P. Hansmann, A. van Roekeghem, L. Vaugier, and S. Biermann, Towards a First-Principles Determination of Effective Coulomb Interactions in Correlated Electron Materials: Role of Intershell Interactions, Phys. Rev. Lett. **119**, 056401 (2017).

[138] P. H. Dederichs, S. Blügel, R. Zeller, and H. Akai, Ground States of Constrained Systems: Application to Cerium Impurities, Phys. Rev. Lett. **53**, 2512 (1984).

[139] M. S. Hybertsen, M. Schlüter, and N. E. Christensen, Calculation of Coulomb-interaction parameters for La_2CuO_4 using a constrained-density-functional approach, Phys. Rev. B **39**, 9028 (1989).

[140] M. T. Czyżyk and G. A. Sawatzky, Local-density functional and on-site correlations: The electronic structure of La_2CuO_4 and $LaCuO_3$, Phys. Rev. B **49**, 14211 (1994).

[141] H. Park, A. J. Millis, and C. A. Marianetti, Total energy calculations using DFT+DMFT: Computing the pressure phase diagram of the rare earth nickelates, Phys. Rev. B **89**, 245133 (2014).

[142] K. Haule, Exact Double Counting in Combining the Dynamical Mean Field Theory and the Density Functional Theory, Phys. Rev. Lett. **115**, 196403 (2015).

[143] W. Metzner and D. Vollhardt, Correlated Lattice Fermions in $d = \infty$ Dimensions, Phys. Rev. Lett. **62**, 324 (1989).

[144] A. Georges and G. Kotliar, Hubbard model in infinite dimensions, Phys. Rev. B **45**, 6479 (1992).

[145] A. Georges, G. Kotliar, W. Krauth, and M. J. Rozenberg, Dynamical mean-field theory of strongly correlated fermion systems and the limit of infinite dimensions, Rev. Mod. Phys. **68**, 13 (1996).

[146] A. Damascelli, Z. Hussain, and Z.-X. Shen, Angle-resolved photoemission studies of the cuprate superconductors, Rev. Mod. Phys. **75**, 473 (2003).

[147] M. Potthoff, M. Aichhorn, and C. Dahnken, Variational Cluster Approach to Correlated Electron Systems in Low Dimensions, Phys. Rev. Lett. **91**, 206402 (2003).

[148] T. Maier, M. Jarrell, T. Pruschke, and M. H. Hettler, Quantum cluster theories, Rev. Mod. Phys. **77**, 1027 (2005).

[149] M. Ferrero *et al.*, Pseudogap opening and formation of Fermi arcs as an orbital-selective Mott transition in momentum space, Phys. Rev. B **80**, 064501 (2009).

[150] A. N. Rubtsov, M. I. Katsnelson, and A. I. Lichtenstein, Dual fermion approach to nonlocal correlations in the Hubbard model, Phys. Rev. B **77**, 033101 (2008).

[151] K. Held, A. A. Katanin, and A. Toschi, Dynamical Vertex ApproximationAn Introduction, Progress of Theoretical Physics Supplement **176**, 117 (2008).

[152] T. Ayral and O. Parcollet, Mott physics and spin fluctuations: A unified framework, Phys. Rev. B **92**, 115109 (2015).

[153] J. Negele and H. Orland, *Quantum many-particle systems*, Frontiers in physics, Addison-Wesley Pub. Co., 1988.

[154] N. V. Prokof'ev and B. V. Svistunov, Polaron Problem by Diagrammatic Quantum Monte Carlo, Phys. Rev. Lett. **81**, 2514 (1998).

[155] A. N. Rubtsov, V. V. Savkin, and A. I. Lichtenstein, Continuous-time quantum Monte Carlo method for fermions, Phys. Rev. B **72**, 035122 (2005).

[156] P. Werner, A. Comanac, L. de' Medici, M. Troyer, and A. J. Millis, Continuous-Time Solver for Quantum Impurity Models, Phys. Rev. Lett. **97**, 076405 (2006).

[157] J. E. Hirsch and R. M. Fye, Monte Carlo Method for Magnetic Impurities in Metals, Phys. Rev. Lett. **56**, 2521 (1986).

[158] M. Aichhorn, S. Biermann, T. Miyake, A. Georges, and M. Imada, Theoretical evidence for strong correlations and incoherent metallic state in FeSe, Phys. Rev. B **82**, 064504 (2010).

[159] A. M. Läuchli and P. Werner, Krylov implementation of the hybridization expansion impurity solver and application to 5-orbital models, Phys. Rev. B **80**, 235117 (2009).

[160] E. Gull, *Continuous-time quantum Monte Carlo algorithms for fermions*, PhD thesis, ETH Zürich, Zürich, 2008.

[161] M. Caffarel and W. Krauth, Exact diagonalization approach to correlated fermions in infinite dimensions: Mott transition and superconductivity, Phys. Rev. Lett. **72**, 1545 (1994).

[162] Y. Lu, M. Höppner, O. Gunnarsson, and M. W. Haverkort, Efficient real-frequency solver for dynamical mean-field theory, Phys. Rev. B **90**, 085102 (2014).

[163] A. Go and A. J. Millis, Adaptively truncated Hilbert space based impurity solver for dynamical mean-field theory, Phys. Rev. B **96**, 085139 (2017).

[164] R. Bulla, T. A. Costi, and T. Pruschke, Numerical renormalization group method for quantum impurity systems, Rev. Mod. Phys. **80**, 395 (2008).

[165] K. A. Hallberg, New trends in density matrix renormalization, Advances in Physics **55**, 477 (2006).

[166] V. Drchal *et al.*, Dynamical correlations in multiorbital Hubbard models: fluctuation exchange approximations, Journal of Physics: Condensed Matter **17**, 61 (2005).

[167] L. V. Pourovskii, M. I. Katsnelson, and A. I. Lichtenstein, Correlation effects in electronic structure of actinide monochalcogenides, Phys. Rev. B **72**, 115106 (2005).

[168] J. Braun, J. Minár, H. Ebert, M. I. Katsnelson, and A. I. Lichtenstein, Spectral Function of Ferromagnetic 3*d* Metals: A Self-Consistent LSDA + DMFT Approach Combined with the One-Step Model of Photoemission, Phys. Rev. Lett. **97**, 227601 (2006).

[169] J. Minár, S. Mankovsky, O. Šipr, D. Benea, and H. Ebert, Correlation effects in fcc-Fe x Ni 1x alloys investigated by means of the KKR-CPA, Journal of Physics: Condensed Matter **26**, 274206 (2014).

[170] G. Kotliar and A. E. Ruckenstein, New Functional Integral Approach to Strongly Correlated Fermi Systems: The Gutzwiller Approximation as a Saddle Point, Phys. Rev. Lett. **57**, 1362 (1986).

[171] L. de'Medici, A. Georges, and S. Biermann, Orbital-selective Mott transition in multiband systems: Slave-spin representation and dynamical mean-field theory, Phys. Rev. B **72**, 205124 (2005).

[172] F. Lechermann, A. Georges, G. Kotliar, and O. Parcollet, Rotationally invariant slave-boson formalism and momentum dependence of the quasiparticle weight, Phys. Rev. B **76**, 155102 (2007).

[173] L. V. Pourovskii, B. Amadon, S. Biermann, and A. Georges, Self-consistency over the charge density in dynamical mean-field theory: A linear muffin-tin implementation and some physical implications, Phys. Rev. B **76**, 235101 (2007).

[174] K. Haule, C.-H. Yee, and K. Kim, Dynamical mean-field theory within the full-potential methods: Electronic structure of $CeIrIn_5$, $CeCoIn_5$, and $CeRhIn_5$, Phys. Rev. B **81**, 195107 (2010).

[175] M. Aichhorn, L. Pourovskii, and A. Georges, Importance of electronic correlations for structural and magnetic properties of the iron pnictide superconductor LaFeAsO, Phys. Rev. B **84**, 054529 (2011).

[176] O. Grånäs *et al.*, Charge self-consistent dynamical mean-field theory based on the full-potential linear muffin-tin orbital method: Methodology and applications, Computational Materials Science **55**, 295 (2012).

[177] H. Park, A. J. Millis, and C. A. Marianetti, Computing total energies in complex materials using charge self-consistent DFT + DMFT, Phys. Rev. B **90**, 235103 (2014).

[178] B. Amadon, S. Biermann, A. Georges, and F. Aryasetiawan, The $\alpha-\gamma$ Transition of Cerium Is Entropy Driven, Phys. Rev. Lett. **96**, 066402 (2006).

[179] B. Amadon, A self-consistent DFT+DMFT scheme in the projector augmented wave method: applications to cerium, Ce_2O_3 and Pu_2O_3 with the Hubbard I solver and comparison to DFT+U, Journal of Physics: Condensed Matter **24**, 075604 (2012).

[180] I. Leonov, V. I. Anisimov, and D. Vollhardt, Metal-insulator transition and lattice instability of paramagnetic V_2O_3, Phys. Rev. B **91**, 195115 (2015).

[181] S. Bhandary, E. Assmann, M. Aichhorn, and K. Held, Charge self-consistency in density functional theory combined with dynamical mean field theory: k-space reoccupation and orbital order, Phys. Rev. B **94**, 155131 (2016).

[182] P. Seth, I. Krivenko, M. Ferrero, and O. Parcollet, TRIQS/CTHYB: A continuous-time quantum Monte Carlo hybridisation expansion solver for quantum impurity problems, Computer Physics Communications **200**, 274 (2016).